

1 **A Bayesian model to correct underestimated 3D wind speeds from sonic anemometers**
2 **increases turbulent components of the surface energy balance**

3

4 John M. Frank^{1,2}, William J. Massman¹, and Brent E. Ewers²

5

6 ¹U.S. Forest Service, Rocky Mountain Research Station, 240 W. Prospect Rd., Fort Collins, CO,
7 80526

8 ²University of Wyoming, Department of Botany and Program in Ecology, 1000 E. University
9 Ave, Laramie, WY, 82071

10

11 *Corresponding author: telephone: +1 970 498 1319; email: jfrank@fs.fed.us

12

13 This paper was written and prepared by a U.S. Government employee on official time, and
14 therefore it is in the public domain and not subject to copyright.

15

16 To be submitted to Atmospheric Measurement Techniques

17

18 **Abstract**

19 Sonic anemometers are the principal instruments in micrometeorological studies of
20 turbulence and ecosystem fluxes. Common designs underestimate vertical wind measurements
21 because they lack a correction for transducer shadowing, with no consensus on a suitable
22 correction. We reanalyze a subset of data collected during field experiments in 2011 and 2013
23 featuring two or four CSAT3 sonic anemometers. We introduce a Bayesian analysis to resolve
24 the three-dimensional correction by optimizing differences between anemometers mounted both
25 vertically and horizontally. A grid of 512 points ($\sim \pm 5^\circ$ resolution in wind location) is defined on
26 a sphere around the sonic anemometer, from which the shadow correction for each transducer-
27 pair is derived from a set of 138 unique state variables **describing the quadrants and borders**.
28 Using the Markov chain Monte Carlo (MCMC) method, the Bayesian model proposes new
29 values for each state variable, recalculates the fast-response dataset, summarizes the five-minute
30 wind statistics, and accepts the proposed new values based on the probability that they make
31 measurements from vertical and horizontal anemometers more equivalent. MCMC chains were
32 constructed for three different prior distributions describing the state variables: no shadow
33 correction, the Kaimal correction for transducer shadowing, and double the Kaimal correction,
34 all initialized with 10% uncertainty. The final posterior correction did not depend on the prior
35 distribution and revealed both self- and cross-shadowing effects from all transducers. After
36 correction, the vertical wind velocity and sensible heat flux increased $\sim 10\%$ with $\sim 2\%$
37 uncertainty, which was significantly higher than the Kaimal correction. We applied the posterior
38 correction to eddy covariance data from various sites across North America and found that the
39 turbulent components of the energy balance (sensible plus latent heat flux) increased on average
40 between 8-12%, with an average 95% credible interval between 6-14%. Considering this is the

41 most common sonic anemometer in the AmeriFlux network and is found widely within
42 FLUXNET, these results provide a mechanistic explanation for much of the energy imbalance at
43 these sites where all terrestrial/atmospheric fluxes of mass and energy are likely underestimated.
44

45 **1. Introduction**

46 The eddy-covariance technique has become the most commonly used method for
47 measuring the ecosystem exchange of mass and energy with the atmosphere. It is fundamental to
48 the global network of flux towers that are central to quantifying terrestrial carbon sinks and
49 sources (Baldocchi, 2003), to hydrological studies accounting for evapotranspiration and
50 sublimation (Biederman et al., 2014; Reba et al., 2012), and to the energy balance through the
51 turbulent fluxes of sensible and latent heat (Welch et al., 2015; Anderson and Wang, 2014).
52 There is a growing consensus within the **micrometeorology and ecosystem** flux communities that
53 many sonic anemometers, the core instrument for all modern eddy-covariance systems,
54 systematically underestimate the vertical wind component (Frank et al., 2016; Horst et al., 2015;
55 Kochendorfer et al., 2012). The ramifications for this are that all vertical fluxes (i.e., carbon
56 dioxide, water vapor, latent heat, sensible heat, momentum) are similarly underestimated for any
57 ecosystem. This **underestimate** is roughly consistent with the persistent energy balance closure
58 problem across flux sites (Leuning et al., 2012; Stoy et al., 2013; Wilson et al., 2002) where a
59 vast majority are assumed to be systematic biased towards low turbulent fluxes of sensible and
60 latent heat.

61 Horst et al. (2015) and Frank et al. (2016) have shown that the error in at least two non-
62 orthogonal sonic anemometer designs can be traced to transducer shadowing that remains
63 uncorrected in the anemometer's firmware. In both studies, shadowing was described a priori by
64 theoretical formulations based on the wind-tunnel tests of Kaimal (1979), yet there was no
65 consensus on a correction. A shortcoming in the use of formulations derived for single
66 transducer-pairs in laminar flow to describe turbulent flow distortions around more complex
67 geometries (Fig. 1) is that shadowing between all transducers and structures cannot be accurately

68 represented or incorporated. A second problem is that in turbulent flow fields there are few
69 standards available to use as a calibration reference. Advancements in Bayesian techniques
70 (Gelman et al., 2014) have created the potential to resolve both of these issues by incorporating
71 prior knowledge of transducer flow distortions with a model that evaluates the omnidirectionality
72 of a sonic anemometer to produce a posterior 3D correction.

73 To quantify a 3D correction of the CSAT3 sonic anemometer, we reanalyze data from
74 field experiments conducted by Frank et al. (2013) and Frank et al. (2016) where wind
75 measurements from non-orthogonal anemometers mounted vertically and horizontally were
76 significantly different. We develop a Bayesian hierarchical model to evaluate three hypotheses:

77 (1) A 3D shadowing correction based solely on wind location can make a non-orthogonal
78 sonic anemometer omnidirectional.

79 (2) This correction increases vertical wind measurements more than expected from single
80 transducer shadowing because it accurately represents all shadowing between transducers.

81 (3) In ecosystems where these instruments are deployed, the application of this correction
82 will result in significantly higher Bayesian credible intervals for the turbulent components of the
83 energy budget and improved surface energy budget closure.

84

85 **2 Methods**

86 **2.1 Reanalysis of field experiments**

87 We reanalyze data from field campaigns conducted by Frank et al. (2013) and Frank et al.
88 (2016). To summarize them, experiments were conducted in 2011 and 2013 where multiple sonic
89 anemometers were deployed in a horizontal array at 24.5 m height on the Glacier Lakes
90 Ecosystem Experiments Site (GLEES) AmeriFlux scaffold above a subalpine forest in

91 southeastern Wyoming, USA (Frank et al., 2014). The anemometers were initially mounted
92 vertically, oriented west, arranged south to north, staggered up and down, and located 0.50 m
93 center-to-center from each other (Fig. 1). Periodically, some of the anemometers were rotated
94 90° around their u -axis and mounted horizontally. In this study we focus only on the CSAT3
95 sonic anemometer (Campbell Scientific, Inc., Logan, UT, USA) during times when both
96 vertically and horizontally mounted anemometers were present (Table 1). All anemometers were
97 operated with firmware version 4.0. It is conventional to describe the three dimensions of a sonic
98 anemometer as the u , v , and w -axes. To reduce confusion in describing horizontal anemometers,
99 we refer to cardinal u , v , and w where the measurements have been rotated to west-east (u),
100 south-north (v), and down-up (w), which are consistent with u , v , and w for vertically mounted
101 anemometers. Finally, because our Bayesian model is computationally intensive we reanalyze a
102 subset of only 5% of the available data (see section 2.3).

103 **2.2 The Bayesian model**

104 Bayesian statistics is based on Bayes theorem (Bayes and Price, 1763), which in modern
105 applications relates the posterior probability of a model parameter conditioned on data to the
106 product of the likelihood of the data and the prior probability of that parameter (Gelman et al.,
107 2014). In essence, the prior represents an initial educated guess or belief in the value of a model
108 parameter, the likelihood is the probability of observing the data if they were deterministically
109 generated from a model, and the posterior is an updated belief in the model parameter
110 considering each the prior, the model, and the data. Analytical evaluation of the posterior is
111 rarely possible, as is in our case, thus the posterior is commonly estimate through the Markov
112 chain Monte Carlo (MCMC) method, Gibbs sampling (Appendix A.1), and the Metropolis-
113 Hastings algorithm (Kruschke, 2010). The framework of our Bayesian model is to divide the

114 sphere around the sonic anemometer into approximately equal grid points and to define a prior
115 probability distribution of the 3D shadowing correction for each transducer pair at each location.
116 Then, the model proposes new corrections for each grid point, recalculates the fast-response
117 dataset, summarizes new five-minute wind statistics, determines the probability that the updated
118 measurements from vertical and horizontal anemometers are more equivalent using the proposed
119 correction versus the old one (i.e., the **Metropolis-Hastings ratio which is** Eq. A13 evaluated for
120 the proposed versus old correction), and finally accepts/rejects the proposal probabilistically
121 from this ratio to construct the posterior correction. The model recursively adjusts the
122 distribution that generates the proposals to achieve between 25 and 50% acceptance rates **which**
123 **are theoretically optimal (Gelman et al., 2014)**. We define a grid of 512 points ($\sim \pm 5^\circ$ resolution
124 of wind location) on a sphere around each of the three transducer pairs of the sonic anemometer.
125 Neglecting the upper and lower mounting arms that extend back into the electronics housing and
126 support block, the CSAT3 is symmetrical on either side of a transducer pair, between the upper
127 and lower hemispheres, and for each of the three transducer pairs. To pool data and reduce
128 computations, we make these assumptions of symmetry to describe all 1,536 points from a set of
129 138 unique state variables.

130 **In our mathematical notation, we use uppercase and lowercase subscripts to distinguish**
131 **variables as scalars, vectors, or matrices. Uppercase subscripts are part of the variable name and**
132 **denote the dimensionality of the variable as well as describe the coordinate system. For example,**
133 **$M_{S \times T}$ is a two dimensional matrix with dimensions S and T , which correspond to sonic and**
134 **transducer coordinates; since there are three dimensions for both coordinate systems this is a 3×3**
135 **matrix. One uppercase subscript by itself denotes a vector in that coordinate system. Lowercase**
136 **subscripts denote indexing for variables that are defined for multiple times or replicate**

137 anemometers; these are essentially multidimensional arrays. When the same letter appears as
 138 both an uppercase and lowercase subscript, this refers to the c^{th} element of dimension C .

139 We test three prior corrections: no shadow correction, the Kaimal correction (Kaimal,
 140 1979; Frank et al., 2016; Horst et al., 2015), and a doubling of the Kaimal correction (Frank et
 141 al., 2016). The Kaimal correction is defined as $U_{T_t} = (1 - 0.16 + 0.16\theta/70)\hat{U}_{T_t}$ for $\theta \leq 70^\circ$ and
 142 $U_{T_t} = \hat{U}_{T_t}$ for $\theta > 70^\circ$, where U_T and \hat{U}_T are the measured and corrected wind velocities in
 143 transducer coordinates and θ is the angle between the wind and the transducer acoustic path, t .

144 The model predicts the standard deviation of the data in cardinal coordinates, σ_C , which is
 145 defined during each five-minute period, f , for each replicate sonic anemometer, i (Fig. 1), from a
 146 normal distribution with mean $\hat{\sigma}_C$ and standard deviation ε (Eq. 1).

$$147 \quad \sigma_{C_{c,f,i}} \sim N(\hat{\sigma}_{C_{c,f,i}}, \varepsilon^{-2}) \quad (1)$$

148 The predicted mean is constructed in several steps. First, the state variable for the 3D correction
 149 in transducer coordinates, α_T , is defined for each grid point, g . Here it does not matter if each grid
 150 point is independent or that they linked together through symmetry. α_T is given a normal prior
 151 probability distribution with mean equal to the prior correction, P , evaluated for each transducer-
 152 pair for wind blowing through the longitude, λ , and latitude, φ , associated with each grid point
 153 and with a predefined standard deviation equal to 0.1, or $\pm 10\%$ uncertainty (Eq. 2).

$$154 \quad \alpha_{T_{t,g}} \sim N(P(t, g), 0.1^{-2}) \quad (2)$$

155 The 3D correction is applied to every 20-Hz sample, j , of the original measured wind velocity
 156 data in transducer coordinates, U_T . The nominal predictor variable, h , selects the corresponding
 157 grid point that occurs with every 20-Hz sample. The corrected 20-Hz wind velocity in transducer
 158 coordinates is \hat{U}_T (Eq. 3).

$$159 \quad \hat{U}_{T_{f,i,j}} = U_{T_{f,i,j}} \cdot \alpha_{T_h} \quad (3)$$

160 The non-orthogonal data are transformed via matrix multiplication into orthogonal sonic
 161 coordinates, \hat{U}_S (Eq. 4).

$$162 \quad \hat{U}_{Sf,i,j} = M_{S \times T} \hat{U}_{Tf,i,j} \quad (4)$$

163 The matrix, $M_{S \times T}$, is specific to the CSAT3 geometry (Eq. 5).

$$164 \quad M_{S \times T} = \begin{bmatrix} -\frac{4}{3} & \frac{2}{3} & \frac{2}{3} \\ 0 & \frac{2}{\sqrt{3}} & -\frac{2}{\sqrt{3}} \\ \frac{2}{3\sqrt{3}} & \frac{2}{3\sqrt{3}} & \frac{2}{3\sqrt{3}} \end{bmatrix} = \begin{bmatrix} -1.333 & 0.667 & 0.667 \\ 0 & 1.155 & -1.155 \\ 0.385 & 0.385 & 0.385 \end{bmatrix} \quad (5)$$

165 For the model to predict data simultaneously from both vertical and horizontal anemometers, a
 166 final corrected time series data set is produced in cardinal coordinates, \hat{U}_C

$$167 \quad \hat{U}_{Cf,i,j} = N_{C \times S_o} \hat{U}_{Sf,i,j} \quad (6)$$

168 The matrix $N_{C \times S_o}$ is straightforward (Eq. 7), and the nominal predictor variable, o , selects the
 169 orientation of every 20-Hz sample.

$$170 \quad N_{C \times S_o} = \begin{cases} \begin{bmatrix} 1 & 0 & 0 \\ 0 & 1 & 0 \\ 0 & 0 & 1 \end{bmatrix}, & o = 1 \text{ (i. e., vertical)} \\ \begin{bmatrix} 1 & 0 & 0 \\ 0 & 0 & -1 \\ 0 & 1 & 0 \end{bmatrix}, & o = 2 \text{ (i. e., horizontal)} \end{cases} \quad (7)$$

171 Using the corrected time series data in cardinal coordinates, the model calculates the
 172 average correction along the three dimensions, β_C , for the five-minute standard deviation data for
 173 each anemometer (Eq. 8).

$$174 \quad \beta_{Cf,i} = \frac{\sqrt{\frac{1}{J-1} \sum_{j=1}^J (\hat{U}_{Cf,i,j} - \frac{1}{J} \sum_{j=1}^J \hat{U}_{Cf,i,j})^2}}{\sqrt{\frac{1}{J-1} \sum_{j=1}^J (U_{Cf,i,j} - \frac{1}{J} \sum_{j=1}^J U_{Cf,i,j})^2}} \quad (8)$$

175 Eq. 8 is equivalent to the ratio of the standard deviation of \hat{U}_C divided by the standard deviation
 176 of U_C , evaluated during each five-minute period for each sonic anemometer. The reference
 177 condition for every five-minute period, $\tilde{\sigma}_C$, is a state variable representing the “true” standard

178 deviation of wind velocity. It is assigned a uniform prior probability distribution that generously
 179 includes the “true” value by allowing each $\tilde{\sigma}_c$ to range from 0 to the maximum of all U_c
 180 measurements (Eq. 9).

$$181 \quad \tilde{\sigma}_{c,f} \sim \text{Unif}(0, \max(U_c)) \quad (9)$$

182 Finally, the model predicts the mean for the standard deviation data as the reference divided by
 183 the average correction (Eq. 10).

$$184 \quad \hat{\sigma}_{c,f,i} = \frac{\tilde{\sigma}_{c,f}}{\beta_{c,f,i}} \quad (10)$$

185 To complete the Bayesian model definition, the model error is a state variable which is
 186 assigned a prior probability distribution with a gamma distribution (Eq. 11).

$$187 \quad \varepsilon \sim \text{Gamma}(1, \hat{b}) \quad (11)$$

188 The variance of the gamma distribution, \hat{b} , is assigned the same variance as the prior distribution
 189 for $\tilde{\sigma}_c$ which is a uniform distribution (Eq. 12).

$$190 \quad \hat{b} = \frac{\sqrt{12}}{\max(U_c) - 0} \quad (12)$$

191 Distributions are defined where normal distributions are $\theta \sim N(a, b)$ with expected value $E(\theta) = a$
 192 and variance $\text{var}(\theta) = 1/b^2$, gamma distributions are $\theta \sim \text{Gamma}(a, b)$ with $E(\theta) = a/b$ and $\text{var}(\theta)$
 193 $= a/b^2$, and uniform distributions are $\theta \sim \text{Unif}(a, b)$ with $E(\theta) = (a+b)/2$ and $\text{var}(\theta) = (b-a)^2/12$.

194 **2.3 Analysis**

195 Our Bayesian analysis was conducted using R (version 3.2.2, (R Core Team, 2015))
 196 within RStudio (version 0.99.486, (RStudio Team, 2015)). We constructed an MCMC chain of
 197 10,000 steps for each of the three priors. Because the Bayesian model estimates are relative and
 198 not an absolute correction (see discussion in section 4.1), we normalized each chain. This was
 199 done in post-processing by dividing α_T by the average of α_T after each time one of the 138 state

200 variables was updated within each MCMC step. We inspected each chain using trace plots and
201 removed the first 500 steps for burn-in and kept 1 out of every 140 steps to eliminate
202 autocorrelation between steps for most grid points (even after reducing to 138 state variables, a
203 few of these were estimated from relatively little data which unavoidably led to high
204 autocorrelation between steps). This reduced each MCMC chain to 68 steps. We conducted
205 several preliminary Bayesian analyses, and used trace plots and tests for autocorrelation to
206 determine that 10,000 steps was sufficient for convergence for most of the 138 state variables
207 defining α_T . Most of these parameters required little or no thinning to reduce autocorrelation
208 between steps and could have remained as MCMC chains with 1,000-10,000 steps. Yet, since the
209 goal was to create a complete 3D correction, we decided to thin all state variables equally. Even
210 though diagnostic tests showed that all parameters, including those with high autocorrelation,
211 appeared to converge within 10,000 steps, it is possible that these chains are still too short for
212 proper convergence. One safeguard against this is confirming that the results from the three
213 chains all result in similar posterior distributions (see section 3.3).

214 Because each MCMC chain was based on a different prior, they are not replicate chains
215 from the same Bayesian analysis. Instead, these are three separate solutions for the posterior
216 correction. But, after considering the results (see section 3.3) and recognizing that, apart from
217 normalization, the prior had minimal influence on the solution, we combined the three priors to
218 create a single chain containing 204 independent samples of the posterior correction. We
219 rescaled the correction to be absolute by forcing the condition that the correction will not change,
220 on average, equatorial wind measurements (i.e., $(u^2 + v^2)^{1/2}$, see discussion in section 4.1). This
221 was done by (1) applying the normalized correction to the time series of vertically mounted
222 anemometers, (2) calculating the corrected five-minute standard deviations for equatorial winds,

223 (3) performing linear regression without an intercept (i.e., model the average change in
224 equatorial winds solely as a scaling factor) between the corrected and uncorrected standard
225 deviations, (4) repeating this for each of the 204 posterior samples, and (5) determining the
226 average of the 204 regression slopes. We divided all values in the normalized 3D correction by
227 this average scaling factor to produce our final posterior correction.

228 Computation of the Bayesian model was extremely intensive: completion of the three
229 chains took upwards of two months of continuous computer processing (Windows 7, Intel®
230 Core™ i7-3630QM CPU @ 2.40 GHz processor, 1 TB solid state hard drive, 20 GB RAM).
231 During beta testing we attempted to estimate the 3D correction independently for all grid points
232 and all transducer pairs, with a single MCMC chain requiring a half-year to complete. Likewise,
233 we investigated increasing the number of grid points to obtain better resolution around the sphere
234 as well as increasing the amount of sonic anemometer data used from the Frank et al. (2013) and
235 Frank et al. (2016) datasets. In both cases we desired an order of magnitude better resolution or
236 more data, but the time required to complete a single MCMC chain quickly made these
237 improvements impractical. Instead, we determined that 512 grid points and 5% of the original
238 data were optimal considering these processing constraints.

239 There is a slight distinction to be made between the prior corrections which are defined as
240 a function, $\alpha_T(\lambda, \varphi)$, of the true longitude and latitude of the wind and the posterior correction
241 which is a function, $\alpha_T(\tilde{\lambda}, \tilde{\varphi})$, where \sim represents the uncorrected sonic anemometer
242 measurement of wind location. This distinction means the posterior correction can be applied
243 directly to the uncorrected raw data whereas the prior should be applied iteratively (i.e., start
244 with the uncorrected observed wind, determine the correction, update the wind measurement,
245 determine the new wind location, update the correction, etc.). To directly compare the prior and

246 posterior corrections, we also present our posterior correction with the wind locations recursively
247 adjusted to approximate the “true” longitude and latitude. For these analyses, we smoothed the
248 posterior **spatially across the grid points** with a spherical spline fit (Wahba, 1981) using R
249 package `mgcv` (Wood, 2006).

250 We quantified the impact of shadowing on measurements of the standard deviations of
251 winds in the three dimensions and the sensible heat flux (H). This was done **iteratively (i.e., for**
252 **each of the 204 posterior samples)** by (1) applying the posterior correction to the **raw** data of
253 vertically mounted anemometers, (2) calculating the five-minute measurements, **and (3)**
254 performing linear regression without an intercept between the corrected and uncorrected
255 measurements. **The 204 regression slopes were combined to form a distribution describing the**
256 **relative change in each of these measurements due to shadowing.** For H , the data **were** planar fit
257 rotated (Lee et al., 2004), time lag adjusted, and vapor flux corrected (Massman and Lee, 2002)
258 using ancillary data from the GLEES AmeriFlux site (Frank et al., 2014).

259 Finally, we quantified the impact of the 3D correction on the sum of the turbulent
260 components of the energy balance (i.e., sensible and latent (LE) heat flux) at various sites across
261 North America (Table 2). Each site featured a CSAT3, a fast-response hygrometer, and ancillary
262 meteorological data. Measurements of LE were calculated similar to H but including the Webb-
263 Pearman-Leuning correction (Webb et al., 1980). The impact of the 3D correction was quantified
264 as a distribution similar to above, except compiled from 30-minute time periods.

265 **2.4 Validation experiment**

266 **We conducted a validation experiment of the posterior 3D correction at the Colorado**
267 **State University, Agricultural Research Development and Education Center (ARDEC), Fort**
268 **Collins, CO, USA (40° 39' 7.9" N 104° 59' 45.7" W) from October 7-14, 2016 . Three CSAT3**

269 sonic anemometers were mounted on an east-west boom 2 m above a pasture of short grass and
270 ~36 m south of a mature corn field. Typical winds at this site are from the north, so in this
271 experiment we refer to cardinal u , v , and w where the measurements have been rotated to north-
272 south (u), west-east (v), and down-up (w). One anemometer (S/N 0869) was vertically mounted
273 in the center of the boom and aimed north, a second (S/N 1560) was 0.62 m to the east and
274 horizontally mounted (i.e., 90° rotation around its u -axis) and aimed north, and a final instrument
275 (S/N 2385) was 0.58 m to the west and mounted askew (Fig. S1). The askew mounting is unique
276 to this validation experiment and can be defined with the unit vectors \mathbf{u} (pointing south), \mathbf{v}
277 (pointing east), and \mathbf{w} (pointing up) as $\mathbf{u}_{\text{askew}} = 2/3\mathbf{u} - 1/3\mathbf{v} - 2/3\mathbf{w}$, $\mathbf{v}_{\text{askew}} = 2/3\mathbf{u} + 2/3\mathbf{v} + 1/3\mathbf{w}$,
278 and $\mathbf{w}_{\text{askew}} = 1/3\mathbf{u} - 2/3\mathbf{v} + 2/3\mathbf{w}$. All wind velocity measurements were converted from sonic to
279 cardinal coordinates, and all tilt angles were measured with a digital level to 0.1° precision such
280 that any mounting imperfections were taken into account. Data were measured at 20 Hz on a
281 CR3000 micrologger (Campbell Scientific, Inc.). In post processing, both the Kaimal correction
282 and the posterior 3D correction were applied to the 20 Hz data. Data were summarized every 5
283 minutes as the standard deviation of wind velocity along the cardinal directions, σ_u , σ_v , and σ_w .
284 Differences between anemometers are presented as root-mean-square of the relative error
285 (RMSE) between measurements from the manipulated anemometers and the vertically mounted
286 one.

287

288 **3 Results**

289 **3.1 No correction**

290 Without any shadow correction applied, measurements between a vertically and a
291 horizontally mounted anemometer were different, which becomes clear when the variance

292 between two vertical anemometers is taken into account (Fig. 2b, d, f versus a, c, e). The root
293 mean square error (RMSE) in the 5-minute standard deviation of wind along all cardinal
294 dimensions (u , v , and w) combined was 9.4% between a vertical and a horizontal anemometer,
295 whereas the same metric between two vertical anemometers was 3.9%. The largest discrepancy
296 was along the cardinal v -axis, where the RMSE increased from 3.7% to 11.1% when comparing
297 vertical and horizontal anemometers (Fig. 2c versus d).

298 **3.2 The Kaimal prior correction**

299 The Kaimal correction is symmetrical with respect to each sonic transducer path (Fig. 3a,
300 c, e). Yet, the same correction when viewed in sonic coordinates reveals unique responses for u ,
301 v , and w (Fig. 3b, d, f). For small latitude winds, the corrections are small for u and v
302 measurements, while those for w are higher yet unstable around the equator (see discussion in
303 section 4.2). When the Kaimal correction was applied to the vertically mounted anemometers,
304 there were minor increases in the 5-minute standard deviations of u and v (0.8% and 2.9%) while
305 the increases for w (5.6%) and H (5.5%) were more substantial. This correction explained some
306 of the differences between vertically and horizontally mounted anemometers (Fig. 4) where the
307 RMSE for all cardinal dimensions combined was 6.2%, or 1.60 times greater than the same error
308 between two vertical anemometers. The discrepancy along the cardinal v -axis decreased to 6.6%,
309 or 1.86 times greater than the same error for two vertical anemometers, though some bias is still
310 apparent (Fig. 4c versus d). While the Kaimal correction is only one of three priors tested in our
311 Bayesian model, it is perhaps the most accepted algorithm currently available to correct
312 transducer shadowing in the CSAT3.

313 **3.3 The Bayesian model**

314 Figure 5 illustrates the approach of the Bayesian model. The model initializes the 512
315 grid points with a prior, in this case the Kaimal correction. No matter the transducer pair or
316 vertical versus horizontal mounting, the 3D correction for all cases are identical but rotated
317 versions of a common correction based on 138 unique state variables. For a single instantaneous
318 wind, the simultaneous corrections for all six combinations of transducer pairs and mounting
319 orientations will be different. As the MCMC chains progress, the Bayesian model will
320 continuously adjust each of the 138 unique state variables so that measurements from the
321 vertically and horizontally mounted anemometers are most similar based on the univariate
322 conditional posterior probability distribution (Eq. A13). Much of the predictive power of the
323 model comes from resolving the inconsistencies along the cardinal v -axis (Fig. 2d) where
324 vertically and horizontally mounted anemometers are likely to be most dissimilar. Specifically, a
325 vertically mounted CSAT3 should measure reasonably correct cross winds which must flow
326 across the entire transducer and support structure of a horizontally mounted CSAT3.

327 Each MCMC chain was initialized with the mean of each prior, yet after convergence
328 their posterior corrections were remarkably similar regardless of the choice of prior correction,
329 with one peculiarity (Fig. 6). There was a clear linear relationship between the prior correction
330 averaged across all 512 grid points (1.000 for no correction, 1.040 for the Kaimal correction, and
331 1.080 for the double-Kaimal correction) and the magnitude of the posterior correction (1.030,
332 1.064, and 1.098, respectively) that relates to the Bayesian model estimating a relative and not
333 absolute correction (see discussion in section 4.1). The posterior correction is more than an
334 estimate of the optimal solution, as it intrinsically accounts for the uncertainty of the correction
335 at each of the 512 grid points (Fig. 7). Whereas each prior was defined with 10% uncertainty
336 (Eq. 2), much of the posterior correction has much lower standard deviations, especially around

337 the transducers where values were as low as 2.5% (Fig. 7a). These uncertainties can be expressed
338 in sonic coordinates for the u , v , and w components, which in general show that the posterior
339 correction is most certain for winds along each of those axes, respectively (Fig. 7b-d), with the
340 uncertainty along the w measurement ranging from 2.7-18.3%.

341 Figure 8 illustrates the completion of the Bayesian model where the same posterior
342 correction is applied to all transducer pairs and both mounting orientations. For every
343 instantaneous wind, application of these six different corrections ultimately results in the 5-
344 minute standard deviations of wind along the cardinal u , v , and w axis being most similar
345 between the two mounting orientations.

346 **3.4 The posterior correction**

347 The posterior correction for each transducer pair is presented in Figure 9. These results
348 take into account the recursive adjustment to the wind locations and have been smoothed with a
349 spherical spline. Significantly more self-shadowing and cross-shadowing around the transducers
350 is visible than compared to the Kaimal prior (Fig. 9a, c, e versus Fig. 3a, c, e, in locations near all
351 transducers). These results are more certain (i.e., low standard deviations when compared to the
352 original 10% assigned to the prior) near the transducers, poorly constrained near the equator (Fig.
353 7a), and independent of the choice of prior correction (Fig. 6). Transforming the posterior
354 correction into sonic coordinates reveals that similar to the Kaimal prior, minimal u and v
355 correction is required for small latitude winds (Fig. 9b, d versus 3b, d). But, the impact of the
356 additional transducer shadowing impacts w measurements far more than was predicted (Fig. 9f
357 versus Fig. 3f) where the posterior was fairly certain for latitudes greater than $\pm 13.5^\circ$ (Fig. 7d);
358 the high uncertainty for near-equatorial wind is discussed in Sect. 4.2. The posterior corrected
359 CSAT3 was the most omnidirectional between vertically and horizontally mounted anemometers

360 (Fig. 10) where the RMSE for all cardinal dimensions combined was 5.3%, or 1.36 times greater
361 than the same error between two vertical anemometers. The discrepancy along the cardinal v -axis
362 was further reduced to 4.4%, which is only 1.20 times greater than the same error for two vertical
363 anemometers, and the bias has been removed (Fig. 10d versus 4d). When the posterior correction
364 was applied to the vertically mounted anemometers there were similar increases to the Kaimal
365 correction in the 5-minute standard deviations of u and v (0.6 ± 0.8 [-1.0 2.2]%, 2.7 ± 0.7 [1.5
366 4.1]%, mean \pm standard deviation [95% credible interval], Fig. 11a-b). But, compared to the
367 Kaimal correction, the increases in w (10.6 ± 1.7 [7.6 13.9]%) and H (9.9 ± 1.6 [7.2 12.6]%)
368 were substantial and significantly higher (Fig. 11c-d). We provide the MCMC chain for the final
369 posterior correction in the supplementary material as a tool for researchers to evaluate in other
370 sonic anemometer studies, to examine the uncertainty in ecosystem flux measurements, and to
371 investigate surface energy balance closure.

372 **3.5 Turbulent components of the ecosystem energy balance across a continent**

373 We applied the posterior correction to various sites across North America that deploy the
374 CSAT3 in their eddy-covariance instrumentation (Table 2). The estimated increase in $H + LE$ at
375 these sites ranged from 8.1-11.6% with an average standard deviation and 95% credible interval
376 of $\pm 1.9\%$ and 6.1-13.8%. For all but one site, the increase in $H + LE$ was significantly higher
377 than the increase due to the Kaimal correction. At the 2 m Yuma, AZ site, the lack of
378 significance is related to anomalously low instantaneous wind latitudes for which the w
379 correction is most uncertain (Fig. 7d).

380 **3.6 Validation of the posterior correction**

381 The validation experiment was conducted during excellent fall weather with no
382 precipitation, where winds averaged $2.0 \pm 1.2 \text{ m s}^{-1}$, maximum sustained gusts were 7.8 m s^{-1} ,

383 38% of the winds were from the northeast (45°) to north-northwest (337.5°), 25% of the winds
384 were from the southeast (135°) to south (180°), and during the other times there were some
385 occasional westerly winds. Results are summarized in Table 3. The RMSE differences between a
386 horizontally mounted anemometer and a vertically mounted anemometer were large (12.6-
387 16.5%) for uncorrected measurements. Applying the Kaimal correction to these anemometers
388 reduced the RMSE differences in σ_u and σ_v (8.5 and 11.4%) but increased the difference in σ_w
389 (17.5%). Compared to the uncorrected data, the average posterior correction decreased the
390 RMSE differences in all directions, though only the reduction in σ_v (8.0-12.2%) was statistically
391 lower (i.e., 95% credible interval). Compared to the Kaimal correction, the average posterior
392 correction was larger for σ_u but lower for σ_v and σ_w , with the reduction in σ_w (11.8-15.9%) being
393 statistically lower than with the Kaimal corrected data. The RMSE differences between an askew
394 mounted anemometer and a vertically mounted anemometer were small/moderate for σ_u and σ_v
395 (6.7% and 11.3%) and large for σ_w (14.7%) for uncorrected measurements. Applying the Kaimal
396 correction to these anemometers reduced the RMSE differences in all directions (4.4-13.5%).
397 The standard deviations for the RMSE differences using the posterior correction was higher for
398 the askew manipulation (1.5-2.4%) than they were for the horizontal manipulation (1.1-1.3%).
399 Compared to the uncorrected data, the average posterior correction increased the RMSE
400 difference for σ_u (8.6%) but decreased the differences for σ_v and σ_w (10.3% and 13.9%), though
401 none of these changes were statistically significant. Compared to the Kaimal correction, the
402 average posterior correction increased the RMSE differences for all directions, with the
403 differences in σ_u (6.2-11.6%) and σ_v (7.2-13.5%) being statistically larger.

404

405 **4 Discussion**

406 **4.1 An omnidirectional standard**

407 Perhaps the most important shortcoming in almost every sonic anemometer study is the
408 lack of a standard wind measurement to compare against. A fundamental problem is that the
409 principle of sonic measurements (Barrett and Suomi, 1949; Kaimal and Businger, 1963) involves
410 the observer effect, i.e. it is virtually impossible for sonic transducers to observe air parcels
411 without influencing them (Buks et al., 1998). Thus, any method that relies on a sonic
412 anemometer measurement as an absolute standard is flawed to an extent. And while we are
413 justified to believe that some sonic anemometer measurements are more accurate than others
414 (Frank et al., 2016) it is tenuous to choose any sonic anemometer measurement as a standard.
415 Then, what are the alternatives? Wind tunnels are extremely useful (Horst et al., 2015; van der
416 Molen et al., 2004) yet it is debatable that such laminar or quasi-laminar calibrations are
417 transferrable to turbulent field conditions (Hogstrom and Smedman, 2004). And, while other new
418 technologies such as Doppler Lidar exist (Sathe et al., 2011; Dellwik et al., 2015) their
419 application as a field reference standard has been limited.

420 What we address is the general problem of determining a calibration given an unknown
421 standard or nothing to compare against. Whether this problem exists in medicine (Lu et al.,
422 1997), acoustics (MacLean, 1940; Monnier et al., 2012), or micrometeorology with respect
423 calibrating sonic anemometry in turbulent flow fields, all approaches have a commonality of
424 testing the relative consistency of a response to unknown signals. In our situation, we hold the
425 3D sonic anemometer to an omnidirectional standard of relative consistency and contend that the
426 correction that best achieves this standard is statistically the most likely 3D calibration. A
427 CSAT3 without any 3D shadow correction is clearly not omnidirectional (Fig 2) as
428 measurements depend on the instrument's orientation. A CSAT3 with the Kaimal transducer

429 shadow correction is better at meeting this standard (Fig 4). However, the posterior 3D
430 correction is remarkably effective in making the CSAT3 omnidirectional (Fig. 10). Because the
431 posterior correction closely achieves the omnidirectional standard, we support our first
432 hypothesis and argue that it is the most accurate correction, in general, for the three dimensions
433 of the CSAT3. Whether or not the posterior correction reveals meaningful information regarding
434 vertical winds and turbulent fluxes is another matter discussed below.

435 A consequence of the omnidirectional standard is that implicitly this produces only
436 relative results. Indeed, our Bayesian posterior has no meaning in an absolute sense without the
437 additional constraint that equatorial winds should be unchanged by the correction. We do not
438 specify the 3D correction at any of the grid points nor we do we specify a reference or “true”
439 condition for the standard deviation of wind during any five minute period. Because of this, the
440 parameter estimates for $\vec{\sigma}_{F \times C}$ and $\vec{\alpha}_{T \times G}$ only have meaning relative to each other. This issue is
441 confounded by the choice of prior distributions which vary dramatically in shape, but produce
442 similar posteriors except for differences in their absolute magnitudes (Fig. 6), i.e., higher
443 magnitude priors produce higher magnitude posteriors. Which absolute magnitude is correct?
444 Without specifying an absolute standard, the answer is none of them. To facilitate comparison
445 and combination of the posteriors we normalized the three MCMC chains.

446 There is a clear need to specify an absolute standard to reference our results. Without
447 one, our normalized posterior correction reduced the 5-minute standard deviations for equatorial
448 winds (i.e., the u - v plane) by 7%. Does this make physical sense? No. The idea that equatorial
449 winds should not be changed is consistent with the expectation that the CSAT3 measures
450 accurate equatorial winds, something that has been demonstrated in both wind tunnels and field
451 campaigns (Yahaya and Frangi, 2004; Friebel et al., 2009). Even the Kaimal correction, which is

452 an absolute correction, predicts $<0.1\%$ error in our measurements of equatorial winds. Because
453 the omnidirectional standard is only relative, we impose an additional absolute standard by
454 defining the average correction for equatorial winds to be zero, which is simply achieved by
455 scaling the normalized posterior correction by 7%. While there certainly is some leeway in this
456 constraint, if the normalized posterior correction were scaled by anything other than $7 \pm 1.4\%$
457 then the correction to horizontal winds would be significantly different (95% credible interval)
458 than both zero and the Kaimal correction (Fig. 11a-b) and would run counter to our belief that
459 the CSAT3 measures reasonable accurate horizontal winds.

460 **4.2 Impact on vertical wind measurements and sensible heat flux**

461 Recent studies have questioned the accuracy of CSAT3 vertical wind velocity
462 measurements (Frank et al., 2013; Kochendorfer et al., 2012) culminating with Horst et al.
463 (2015) and Frank et al. (2016) who identified the anemometer's lack of transducer shadowing
464 correction as the root cause. Quantifying the inaccuracy and determining how to fix this problem
465 has been a challenge. While each of these studies estimated different errors in w at their field
466 sites (3.5% (Horst et al., 2015), 6-10% (Frank et al., 2013), 5.5-12.5% (Frank et al., 2016), and
467 14% (Kochendorfer et al., 2012)), it wasn't until Horst et al. (2015) proposed the application of
468 the Kaimal correction (Kaimal, 1979) that a mechanistic explanation was used to quantify the
469 underestimate. Whether or not the Kaimal correction is sufficient is a matter of debate, but it
470 currently represents the best prior knowledge to explain the CSAT3's shortcomings.

471 Solely because the posterior correction makes the CSAT3 more omnidirectional does not
472 imply that field measurements of vertical wind and turbulent fluxes are impacted, nor does this
473 assure that these impacts would be due to anything more than chance. Even with the uncertainty
474 in the posterior w correction explicitly quantified (Fig. 7d) it is difficult to foresee if w is

475 significantly impacted without applying the posterior correction to actual data. A powerful
476 attribute of the Bayesian analysis is that the posterior correction can be applied to raw data to
477 produce probability distribution estimates for w and H from which statistical inferences can be
478 made. Using GLEES data, Fig. 11c-d confirms that to achieve an omnidirectional sensor (Fig.
479 10) with minimal change to horizontal winds (Fig. 11a-b) the required correction will increase
480 both w and H by an average of 10.6% and 9.9%, which is significantly more (>95% credible
481 interval) than predicted by the Kaimal prior. We argue that this significant increase in the vertical
482 wind occurs because the posterior correction more accurately accounts for all shadowing
483 between transducers (Fig. 9 versus Fig. 3), therefore we support our second hypothesis.

484 Also of note, there are instabilities in the prior and posterior w corrections for near-
485 equatorial winds that occur at latitudes less than $\pm 4^\circ$ (6 inflection points around the equator, Fig.
486 3f and 9f). The mathematical cause for these instabilities and the locations of the inflection
487 points are derived in Appendix A.2, and unless the corrections for the three transducers are
488 exactly equal everywhere around the equator these instabilities will exist. The existence of these
489 instabilities should cause concern for eddy-covariance measurements. The ultimate impact of this
490 phenomena is difficult to know, because on one hand, w for latitudes less than $\pm 4^\circ$ are by
491 definition very small, but on the other, these eddies constitute a large proportion of winds that
492 exist under field conditions and their correction is currently unpredictable. For example, at
493 GLEES 30% of winds occur at latitudes within $\pm 4^\circ$ (unpublished analysis of Figure 4 from Frank
494 et al. (2016)). It is unknown how aggressively the correction for these winds approaches $\pm\infty$ or if
495 more inflection points actually occur. For all non-orthogonal geometries, not just the CSAT3, if
496 any transducer shadowing occurs at the equator, there will be instabilities in the w correction.

497 **4.4 Impact across global flux networks**

498 Energy balance is a fundamental ecosystem concept where the flow of available energy
499 into an ecosystem influences the microclimate, drives photosynthesis, and establishes trophic
500 levels among the biota (Odum, 1957; Fisher and Likens, 1973; Teal, 1962). Yet, eddy covariance
501 studies of ecosystem fluxes seldom delve into details of energy flow beyond the generation of
502 sensible and latent heat. It is often stated that most eddy covariance sites underestimate these
503 turbulent components of the energy balance by 10-20% when compared to the available energy
504 (Wilson et al., 2002; Foken, 2008; Stoy et al., 2013; Leuning et al., 2012; Franssen et al., 2010).
505 Even when sites thoroughly account for lesser components such as energy stored in the biomass
506 or canopy air, the turbulent energy can still be 1-14% underestimated (Heilman et al., 2009;
507 Oliphant et al., 2004; Barr et al., 2006; Wang et al., 2012). It is common for sites to deal with
508 this problem by forcing energy balance closure by increasing H and/or LE (Heilman et al., 2009;
509 Oliphant et al., 2004; Twine et al., 2000; Scott et al., 2004) or even carbon fluxes (Barr et al.,
510 2006) by the percent of the energy imbalance. Is there a mechanistic reason why so many sites
511 believe their turbulent fluxes are underestimated? While it is difficult to generalize for every site,
512 one similarity among these studies (Heilman et al., 2009; Oliphant et al., 2004; Barr et al., 2006;
513 Wang et al., 2012; Twine et al., 2000; Scott et al., 2004) is they all feature a CSAT3, as do ~60%
514 of all sites in the AmeriFlux network (unpublished summary of 150 the 228 sites where
515 anemometer information was available, list accessed at <http://ameriflux.lbl.gov/> in November
516 2015) and numerous sites distributed across the world within FLUXNET
517 (<http://fluxnet.fluxdata.org/>).

518 After applying the posterior correction to the CSAT3 at our site, measurements of one of
519 the energy balance components, H , increased $9.9 \pm 1.6\%$, which is about twice the 5.5% increase
520 predicted the Kaimal correction (Fig. 11) (note, the field experiments were conducted without a

521 co-located fast-response hygrometer, hence we do not estimate the impact on *LE* at our site).
522 However, we must consider that our field site in Wyoming is unusual, with extreme wind and
523 turbulence, and where summer friction velocity (u_*) averages 0.6 m s^{-1} (Frank et al., 2016).
524 While this made GLEES a good location to conduct the turbulent field experiments that led to
525 the development of the posterior correction, do our results lead to similar impacts on ecosystem
526 fluxes elsewhere? To answer this we applied the posterior correction to eddy covariance
527 measurements at various sites across North America that employ the CSAT3 (Table 2). We
528 found that the sum of the turbulent components of the energy balance (sensible plus latent heat
529 flux) increased on average between 8-12% with the average 95% credible interval being 6-14%.
530 At most sites this was significantly higher than applying the Kaimal correction. Thus, it is highly
531 probable that at flux sites that employ the CSAT3 sonic anemometer the posterior correction will
532 significantly increase the turbulent components of the energy budget and explain much of the
533 ubiquitous energy imbalance problem; therefore we support our third hypothesis.

534 Are the results from this study applicable to the non-orthogonal sonic anemometers
535 produced by other manufacturers? Possibly. Frank et al. (2016) showed that the Applied
536 Technologies, Inc. A-probe shares a similar transducer geometry, a lack of a shadow correction
537 algorithm, and similar differences between vertically and horizontally mounted anemometers, so
538 it would be reasonable to expect a similar 3D correction for that instrument. But other
539 manufacturers do apply wake corrections in their firmware that are traceable to wind tunnel
540 calibrations. Are these adequate? Maybe not, as non-orthogonal anemometers from other
541 manufacturers have been implicated to erroneously measure the vertical wind (Kochendorfer et
542 al., 2012; Nakai et al., 2014; Nakai and Shimoyama, 2012). Without details of the calibrations or
543 the wake corrections it is difficult to know. Regardless, for any non-orthogonal sonic

544 anemometer with vertically oriented transducers, equatorial instabilities are likely to exist
545 (Appendix A.2) that would be extremely difficult to characterize with only a series of wind
546 tunnel calibrations. One benefit of our methodology is that it allows an independent check on the
547 sufficiency of these wake corrections. If such an instrument fails to consistently measure 3-
548 dimensional winds (i.e., it responds like Fig. 2), then our methodology would estimate a
549 posterior correction that could correct a wake-corrected anemometer. Because ~90% of all
550 AmeriFlux sites use non-orthogonal sonic anemometers (Frank et al., 2013; Nakai et al., 2014), it
551 would be appropriate to investigate this issue for all non-orthogonal sonic anemometer designs.

552 **4.5 The next step**

553 While these results reveal much about the nature of shadowing in a non-orthogonal sonic
554 anemometer, there is much more to be done. First, due to the intense computational burden of
555 this analysis we never fully utilized our data. While we only analyzed 5% of the available data,
556 limited the 3D correction to approximately $\pm 5^\circ$ resolution and only 138 unique corrections, and
557 terminated the Bayesian MCMC chains after only 10,000 steps, it still took months of continuous
558 processing with extensive memory usage to produce these results. Obviously there is an
559 opportunity to adapt this analysis to run on multiple cores or a supercomputer. As we developed
560 our analysis it became apparent that with more data the standard deviations of the posterior
561 distribution improved; we foresee that with 20 times more data the uncertainty in the posterior
562 correction would be further reduced. Adaptation to a high-performance computer will allow for a
563 more precise grid, longer MCMC chains, and a lower standard deviation of the posterior
564 distribution.

565 Our results draw extensively on the symmetry of the CSAT3, which fails to account for
566 the upper and lower mounting arms that extend back into the electronics housing and support

567 block. We beta tested our model to solve for the 3D correction independently for each transducer
568 and for all grid points around the sphere. We abandoned this because winds at GLEES are fairly
569 unidirectional causing many of the grid points to be poorly characterized. Plus with an order of
570 magnitude more unique grid points to solve, the computation took over 5 months to complete
571 just one MCMC chain! There is a middle ground between assuming symmetry and pooling data,
572 i.e., the correction for the A transducer pair could be considered symmetrical along the $u-w$ plane
573 and the corrections for transducer pairs B and C are mirror images of each other. In addition to
574 solving the problem with less assumptions of symmetry, more experimental manipulations
575 should be tested. We only tested a 90° rotation along the u -axis, but there are limitless other
576 manipulations that would help characterize the shadowing around the entire 3D space
577 surrounding an anemometer. Our model could easily be adapted to handle different
578 manipulations using Eq. (7). This equation can be expanded to account for a limitless number of
579 manipulations within the same analysis.

580 Sonic anemometer corrections should be verified and validated. There is an opportunity
581 to statistically cross-validate the posterior 3D correction with subsets of the other 95% of
582 available data; we decided against this because the 5% used was already partitioned equally
583 throughout the full dataset, plus, analyzing multiple rounds of training and validation datasets
584 would take additional months of computation. Instead of a statistical cross-validation analysis,
585 we conducted a validation field experiment to determine if (1) our results are reproducible and
586 (2) if they can explain other manipulations. From this, we first conclude that our results are
587 reproducible. In both our main experiments at GLEES and the validation experiment at ARDEC,
588 there was improved agreement between vertically and horizontally mounted anemometers when
589 using the posterior correction versus the Kaimal correction or no-correction (Table 3). The

590 largest differences between anemometers was for σ_v (11.1% and 16.5%, Fig. 2d, Table 3) which
591 were reduced with the Kaimal correction (6.6% and 11.4%, Fig. 4d, Table 3) and then further
592 improved with the posterior correction (4.4% and 9.8%, Fig. 10d, Table 3). In both analyses, the
593 differences in σ_u were reduced with either correction, but the best performance was the Kaimal
594 prior (Figs. 4b versus 10b, Table 3). Finally, in both cases the differences in σ_w were smallest
595 using the posterior correction (Figs. 4f versus 10f, Table 3). Moreover, we justify our validation
596 because it involved an independent dataset that was collected at a different field site, over
597 radically different terrain and vegetation, and using anemometers with different serial numbers.
598 We are less confident that our posterior correction can explain all manipulations. The differences
599 in σ_u and σ_v between vertically and askew mounted anemometers were significantly better with
600 the Kaimal correction (Table 3). It is important to note, however, that these differences were the
601 smallest of all the comparisons (Uncorrected column in Table 3); i.e., it may be inconsequential
602 that the Kaimal correction outperforms the posterior correction for measurements that were fairly
603 good to begin with. Meanwhile, the difference in σ_w was large, though it is unclear if the
604 posterior correction makes this significantly better or worse (Table 3). This lack of clarity means
605 the askew manipulation cannot be used to validate or falsify the posterior correction. This is not
606 surprising, because the posterior correction was estimated without data from or knowledge of
607 such a unique manipulation, and as it is, much of the posterior correction contains a large
608 uncertainty (Fig. 7a). Though the posterior correction is too uncertain to explain the askew
609 manipulation, this does not mean our estimates of $H + LE$ at various field sites are flawed
610 because these estimates account for the fact that much of the posterior is uncertain. We expect
611 that expanding our Bayesian analysis to include data from more manipulations, e.g. the askew

612 example, would further constrain the regions of uncertainty found in the current posterior
613 correction.

614 Our results using the posterior correction (Fig. 10) show that there is still unexplained
615 residual error, though we expect some of this to be reduced with our suggestions above. While
616 Horst et al. (2015) showed that to a first order that transducer shadowing is a function of the
617 longitude and latitude of the instantaneous wind, the impact of other covariates such as wind
618 velocity and turbulence may need to be considered. An advantage of performing our analysis in a
619 Bayesian framework is that the model can be expanded to incorporate the effects of these
620 covariates.

621 And finally, our posterior correction and methodology should be compared to other
622 independent analysis of sonic anemometer shadowing such as wind tunnel data (Horst et al.,
623 2015) or an independent Doppler Lidar system (Sathe et al., 2011). Care should be taken when
624 incorporating these results, as anemometers could respond differently under laminar flow in a
625 wind tunnel versus under turbulent field conditions. Regardless, a key to resolving this problem
626 will be to embrace new technologies, new experimental designs, and new analyses.

627

628 **5 Conclusion**

629 The non-orthogonal CSAT3 sonic anemometer produces different results (Fig. 2) when it
630 is mounted horizontally instead of vertically (Fig. 1). Assuming that the primary source of this
631 error is shadowing across the various transducers, a Bayesian model can estimate a posterior
632 correction (Fig. 8) that ultimately makes measurements from vertically and horizontally mounted
633 anemometers most similar (Fig. 10). Even when taking into account the uncertainty of the
634 posterior correction (Fig. 7) the increases in vertical wind velocity and sensible heat flux

635 measurements are significantly larger and are approximately twice the magnitude of the Kaimal
636 correction (Fig. 11). When this posterior correction is applied to various eddy covariance sites
637 across North America, the turbulent components of the ecosystem energy balance (sensible plus
638 latent heat flux) increased between 8.1-11.6%, with an average 95% confidence that this increase
639 was between 6.1-13.8% (Table 2). Considering this is the most common sonic anemometer in the
640 AmeriFlux network and is found in all the regional networks that comprise FLUXNET, these
641 results have major implications for countless studies that use the eddy-covariance technique to
642 measure terrestrial/atmospheric exchange of mass and energy.

643

644 **Acknowledgments**

645 We thank Jorge Ramirez, Susan Howe, Mario Bretfeld, Kelly Elder, Banning Starr, Bill
646 Kustas, and Joe Alfieri for providing data from their unique field sites. We especially thank Ben
647 Bird for his **comments and** countless hours of statistical advice in developing the Bayesian
648 model. **We thank Jay Ham for his generous assistance in conducting the field validation**
649 **experiment. We thank Bob Hall and the two anonymous reviewers whose thoughts and**
650 **comments improved this manuscript.** This study was funded by the U.S. Forest Service, the
651 Wyoming Water Development Commission, the USGS, the NSF (awards EPS-1208909 and
652 EAR-0444053), and the DOD Army Research Office (W911NF-05-1-0558 and W911NF-05-1-
653 0126).

654

655 **Appendix**

656 **A.1 Univariate conditional posterior distribution functions for Gibbs sampling**

657 For the univariate conditional posterior distribution functions there is a distinction
 658 between independent grid points versus those linked together through symmetry. In the case of
 659 the former, these functions can be evaluated for each unique grid point, g , for each transducer
 660 pair, t . In the case of the latter, g and t refer to the sets of all grid points and transducers that
 661 share the same unique state variable for their shadow correction, and these functions can be
 662 applied to each of these unique sets.

663 First, using Bayes Theorem, the joint posterior distribution of the model parameters can
 664 be expressed as being proportional to the product of the likelihood of the data and the joint prior
 665 distribution of the model parameters (Eq. A1).

$$666 \quad p(\tilde{\sigma}_C, \alpha_T, \varepsilon | \sigma_C) \propto p(\sigma_C | \tilde{\sigma}_C, \alpha_T, \varepsilon) p(\tilde{\sigma}_C, \alpha_T, \varepsilon) \quad (\text{A1})$$

667 Because the prior distributions for three model parameters are independent, the joint prior
 668 distribution can be written as the product of the individual probabilities (Eq. A2).

$$669 \quad p(\tilde{\sigma}_C, \alpha_T, \varepsilon | \sigma_C) \propto p(\sigma_C | \tilde{\sigma}_C, \alpha_T, \varepsilon) p(\tilde{\sigma}_C) p(\alpha_T) p(\varepsilon) \quad (\text{A2})$$

670 The likelihood of the data is normally distributed (Eq. A3).

$$671 \quad p(\sigma_C | \tilde{\sigma}_C, \alpha_T, \varepsilon) = \frac{1}{\sqrt{2\pi\varepsilon}} e^{\left(-\frac{1}{2\varepsilon^2}(\sigma_C - \hat{\sigma}_C)^2\right)} \quad (\text{A3})$$

672 Because $\hat{\sigma}_C$ is both a function of $\tilde{\sigma}_C$ and α_T the likelihood is indeed a function of all three model
 673 parameters. The individual prior distributions for $\tilde{\sigma}_C$, α_T , and ε are uniformly (Eq. A4), normally
 674 (Eq. A5), and gamma (Eq. A6) distributed, respectively.

$$675 \quad p(\tilde{\sigma}_C) = \begin{cases} \frac{1}{\max(U_C)}, & 0 \leq \tilde{\sigma}_C \leq \max(U_C) \\ 0, & \text{otherwise} \end{cases} \quad (\text{A4})$$

$$676 \quad p(\alpha_{T,t,g}) = \frac{1}{\sqrt{2\pi}(0.1)} e^{\left(-\frac{1}{2(0.1)^2}(\alpha_{T,t,g} - P(t,g))^2\right)} \quad (\text{A5})$$

$$677 \quad p(\varepsilon) = b e^{-b\varepsilon} \quad (\text{A6})$$

678 Gibbs sampling for each model parameter is based on the univariate conditional posterior
679 distribution which assumes that all other model parameters plus the data are given (in the case of
680 sampling within a multidimensional array, all other parameters within that array are given except
681 the one at the index being evaluated). For $\tilde{\sigma}_c$ the univariate conditional posterior distribution can
682 be expressed as a form of Bayes Theorem (Eq. A7).

$$683 \quad p\left(\tilde{\sigma}_{c,f} \mid \underline{\tilde{\sigma}}_{-c,f}, \underline{\alpha}_T, \varepsilon, \underline{\sigma}_c\right) = \frac{p\left(\underline{\tilde{\sigma}}_c, \underline{\alpha}_T, \varepsilon \mid \underline{\sigma}_c\right) p\left(\underline{\sigma}_c\right)}{p\left(\underline{\tilde{\sigma}}_{-f,c}, \underline{\alpha}_T, \varepsilon, \underline{\sigma}_c\right)} \quad (\text{A7})$$

684 The under-bar denotes all elements within a multidimensional array, while the notation $\underline{\tilde{\sigma}}_{-c,f}$
685 means all elements of $\tilde{\sigma}_c$ except for $\tilde{\sigma}_{c,f}$. On right side of Eq. A7, both the second term in the
686 numerator and the denominator are assumed given and can be omitted if the equal sign is
687 changed to a proportional sign. The first term in the numerator, $p\left(\underline{\tilde{\sigma}}_c, \underline{\alpha}_T, \varepsilon \mid \underline{\sigma}_c\right)$, is the joint
688 posterior distribution summed across all parameters (Eq. A8).

$$689 \quad p\left(\underline{\tilde{\sigma}}_c, \underline{\alpha}_T, \varepsilon \mid \underline{\sigma}_c\right) \propto$$

$$690 \quad \prod_{c=1}^3 \prod_{f=1}^F \left\{ \left[\prod_{i=1}^I p\left(\sigma_{c,f,i} \mid \tilde{\sigma}_{c,f}, \alpha_T, \varepsilon\right) \right] p\left(\tilde{\sigma}_{c,f}\right) \right\} \prod_{t=1}^3 \prod_{g=1}^G p\left(\alpha_{T,t,g}\right) p\left(\varepsilon\right) \quad (\text{A8})$$

691 Assuming that all but $\tilde{\sigma}_{c,f}$ is given plus requiring that the proposed value for $\tilde{\sigma}_{c,f}$ is within the
692 valid range (i.e., $p\left(\tilde{\sigma}_{c,f}\right)$ is constant and can be omitted) Eq. A7 simplifies to Eq. A9.

$$693 \quad p\left(\tilde{\sigma}_{c,f} \mid \underline{\tilde{\sigma}}_{-c,f}, \underline{\alpha}_T, \varepsilon, \underline{\sigma}_c\right) \propto \prod_{i=1}^I p\left(\sigma_{c,f,i} \mid \tilde{\sigma}_{c,f}, \alpha_T, \varepsilon\right) \quad (\text{A9})$$

694 Substituting in the likelihood from Eq. A3 and simplifying gives the univariate conditional
695 posterior distribution for $\tilde{\sigma}_{c,f}$ (Eq. A10).

$$696 \quad p\left(\tilde{\sigma}_{c,f} \mid \underline{\tilde{\sigma}}_{-c,f}, \underline{\alpha}_T, \varepsilon, \underline{\sigma}_c\right) \propto e^{\left(-\frac{1}{2\varepsilon^2} \sum_{i=1}^I \left(\sigma_{c,f,i} - \tilde{\sigma}_{c,f}\right)^2\right)} \quad (\text{A10})$$

697 The univariate conditional posterior distribution for α_T can be expressed as Bayes Theorem (Eq.
698 A11).

$$699 \quad p\left(\alpha_{T_{t,g}} \mid \underline{\tilde{\sigma}}_C, \underline{\alpha}_{T_{-t,g}}, \varepsilon, \underline{\sigma}_C\right) = \frac{p(\underline{\tilde{\sigma}}_C, \underline{\alpha}_T, \varepsilon \mid \underline{\sigma}_C) p(\underline{\sigma}_C)}{p(\underline{\tilde{\sigma}}_C, \underline{\alpha}_{T_{-t,g}}, \varepsilon, \underline{\sigma}_C)} \quad (\text{A11})$$

700 Again, only the first term in the numerator must be evaluated while assuming that all but $\alpha_{T_{t,g}}$
701 are given (Eq. A12).

$$702 \quad p\left(\alpha_{T_{t,g}} \mid \underline{\tilde{\sigma}}_C, \underline{\alpha}_{T_{-t,g}}, \varepsilon, \underline{\sigma}_C\right) \propto \prod_{c=1}^3 \prod_{f=1}^F \prod_{i=1}^I p\left(\sigma_{C_{c,f,i}} \mid \underline{\tilde{\sigma}}_{C_{c,f}}, \alpha_T, \varepsilon\right) p\left(\alpha_{T_{t,g}}\right) (\text{A12})$$

703 Substituting in both the likelihood of the data (Eq. A3) and the prior distribution for $\alpha_{T_{t,g}}$ (Eq.
704 A5) and simplifying yields the univariate conditional posterior distribution for $\alpha_{T_{t,g}}$ (Eq. A13).

$$705 \quad p\left(\alpha_{T_{t,g}} \mid \underline{\tilde{\sigma}}_C, \underline{\alpha}_{T_{-t,g}}, \varepsilon, \underline{\sigma}_C\right) \propto e^{\left(-\frac{1}{2\varepsilon^2} \sum_{c=1}^3 \sum_{f=1}^F \sum_{i=1}^I (\sigma_{C_{c,f,i}} - \hat{\sigma}_{C_{c,f,i}})^2 - \frac{1}{2(0.1)^2} (\alpha_{T_{t,g}} - P(t,g))^2\right)}$$

706 (A13)

707 An important issue is that $\hat{\sigma}_C$ is a function of α_T and must be evaluated for every proposed
708 change to the 3D correction. This is computationally intensive and causes a bottleneck in the
709 analysis. Finally, the univariate conditional posterior distribution for ε can be expressed as Bayes
710 Theorem (Eq. A14).

$$711 \quad p\left(\varepsilon \mid \underline{\tilde{\sigma}}_C, \underline{\alpha}_T, \underline{\sigma}_C\right) = \frac{p(\underline{\tilde{\sigma}}_C, \underline{\alpha}_T, \varepsilon \mid \underline{\sigma}_C) p(\underline{\sigma}_C)}{p(\underline{\tilde{\sigma}}_C, \underline{\alpha}_T, \underline{\sigma}_C)} \quad (\text{A14})$$

712 Only the first term in the numerator must be evaluated while assuming that all but ε are given
713 (Eq. A15).

$$714 \quad p\left(\varepsilon \mid \underline{\tilde{\sigma}}_C, \underline{\alpha}_T, \underline{\sigma}_C\right) \propto \prod_{c=1}^3 \prod_{f=1}^F \prod_{i=1}^I p\left(\sigma_{C_{c,f,i}} \mid \underline{\tilde{\sigma}}_{C_{c,f}}, \alpha_T, \varepsilon\right) \quad (\text{A15})$$

715 Substituting in the likelihood from Eq. A3 and simplifying yields the univariate conditional
716 posterior distribution for ε (Eq. A16)

717
$$p \left(\varepsilon \left| \underline{\tilde{\sigma}}_C, \underline{\alpha}_T, \underline{\sigma}_C \right. \right) \propto \varepsilon^{-3Fl} e^{\left(-\frac{1}{2\varepsilon^2} \sum_{c=1}^3 \sum_{f=1}^F \sum_{i=1}^I (\sigma_{C,f,i} - \tilde{\sigma}_{C,f,i})^2 \right)} \quad (\text{A16})$$

718 **A.2 Instability in the w correction for near equatorial winds**

719 For a CSAT3, the amount of correction applied to the vertical wind velocity, expressed as
 720 the individual corrections $\alpha_A(\lambda, \varphi)$, $\alpha_B(\lambda, \varphi)$, and $\alpha_C(\lambda, \varphi)$ for the three transducer pairs A, B,
 721 and C as functions of longitude, λ , and latitude, φ , is:

722
$$\frac{w_{corrected}}{w_{uncorrected}} = \frac{2}{3\sqrt{3}} \left[\left(-\frac{\cos \lambda}{2 \tan \varphi} + \frac{\sqrt{3}}{2} \right) \alpha_A(\lambda, \varphi) + \left(\frac{\cos \lambda + \sqrt{3} \sin \lambda}{4 \tan \varphi} + \frac{\sqrt{3}}{2} \right) \alpha_B(\lambda, \varphi) + \left(\frac{\cos \lambda - \sqrt{3} \sin \lambda}{4 \tan \varphi} + \frac{\sqrt{3}}{2} \right) \alpha_C(\lambda, \varphi) \right] \quad (\text{A17})$$

724 If the individual corrections for the three transducer pairs never approach 0 or $\pm\infty$, which is a
 725 safe assumption considering they are always around 1 (Figs. 3a, c, e and 9a, c, e), the limit of this
 726 as the latitude approaches the equator is:

727
$$\lim_{\varphi \rightarrow 0} \frac{w_{corrected}}{w_{uncorrected}} = \frac{1}{3} (\alpha_A(\lambda, 0^\circ) + \alpha_B(\lambda, 0^\circ) + \alpha_C(\lambda, 0^\circ)) +$$

 728
$$\frac{2}{3\sqrt{3}} \left[\left(-\frac{\cos \lambda}{2} \right) \alpha_A(\lambda, 0^\circ) + \left(\frac{\cos \lambda + \sqrt{3} \sin \lambda}{4} \right) \alpha_B(\lambda, 0^\circ) + \left(\frac{\cos \lambda - \sqrt{3} \sin \lambda}{4} \right) \alpha_C(\lambda, 0^\circ) \right] \lim_{\varphi \rightarrow 0} \frac{1}{\tan \varphi} \quad (\text{A18})$$

729 This approaches $\pm\infty$ unless the terms associated with the limit of the tangent exactly cancel. This
 730 is achieved if $\alpha_A(\lambda, 0^\circ) = \alpha_B(\lambda, 0^\circ) = \alpha_C(\lambda, 0^\circ)$, which includes the special case where
 731 $\alpha_A(\lambda, 0^\circ) = \alpha_B(\lambda, 0^\circ) = \alpha_C(\lambda, 0^\circ) = 1$. Based on our assumptions of symmetry with the
 732 CSAT3, $\alpha_B(\lambda, \varphi) = \alpha_A(60^\circ - \lambda, -\varphi)$ and $\alpha_C(\lambda, \varphi) = \alpha_A(60^\circ + \lambda, -\varphi)$. Therefore, the w
 733 correction for near equatorial winds is unstable unless:

734
$$\alpha_A(\lambda, 0^\circ) = \frac{1 + \sqrt{3} \tan \lambda}{2} \alpha_A(60^\circ - \lambda, 0^\circ) + \frac{1 - \sqrt{3} \tan \lambda}{2} \alpha_A(60^\circ + \lambda, 0^\circ) \quad (\text{A19})$$

735 This is satisfied by $\lambda = 30^\circ, 90^\circ, 150^\circ, 210^\circ, 270^\circ$, and 330° . Eq. A19 shows that if the weighted
 736 average of $\alpha_A(60^\circ - \lambda, -\varphi)$ and $\alpha_A(60^\circ + \lambda, -\varphi)$ cancel $\alpha_A(\lambda, 0^\circ)$ then the correction will be
 737 stable. This cannot be achieved if the correction $\alpha_A(\lambda, 0^\circ)$ is monotonic between $0^\circ \leq \lambda \leq 90^\circ$.

738 Because the w correction is symmetric every 30° , any solution besides $\lambda = 30^\circ, 90^\circ, 150^\circ, 210^\circ,$

739 $270^\circ,$ and 330° will be mirrored 12 times.

740

741 **References**

- 742 Anderson, R. G., and Wang, D.: Energy budget closure observed in paired eddy covariance
743 towers with increased and continuous daily turbulence, *Agricultural and Forest*
744 *Meteorology*, 184, 204-209, doi: 10.1016/j.agrformet.2013.09.012, 2014.
- 745 Baldocchi, D. D.: Assessing the eddy covariance technique for evaluating carbon dioxide
746 exchange rates of ecosystems: past, present and future, *Glob. Change Biol.*, 9, 479-492,
747 doi: 10.1046/j.1365-2486.2003.00629.x, 2003.
- 748 Barr, A. G., Morgenstern, K., Black, T. A., McCaughey, J. H., and Nesic, Z.: Surface energy
749 balance closure by the eddy-covariance method above three boreal forest stands and
750 implications for the measurement of the CO₂ flux, *Agricultural and Forest Meteorology*,
751 140, 322-337, doi: 10.1016/j.agrformet.2006.08.007, 2006.
- 752 Barrett, E. W., and Suomi, V. E.: Preliminary report on temperature measurement by sonic
753 means, *Journal of Meteorology*, 6, 273-276, doi: doi:10.1175/1520-
754 0469(1949)006<0273:PROTMB>2.0.CO;2, 1949.
- 755 Bayes, M., and Price, M.: An Essay towards solving a problem in the doctrine of chances. By the
756 Late Rev. Mr. Bayes, F. R. S. Communicated by Mr. Price, in a letter to John Canton, A.
757 M. F. R. S, *Philosophical Transactions*, 53, 370-418, doi: 10.1098/rstl.1763.0053, 1763.
- 758 Biederman, J. A., Harpold, A. A., Gochis, D. J., Ewers, B. E., Reed, D. E., Papuga, S. A., and
759 Brooks, P. D.: Increased evaporation following widespread tree mortality limits
760 streamflow response, *Water Resour. Res.*, 50, 5395-5409, doi: 10.1002/2013wr014994,
761 2014.
- 762 Buks, E., Schuster, R., Heiblum, M., Mahalu, D., and Umansky, V.: Dephasing in electron
763 interference by a 'which-path' detector, *Nature*, 391, 871-874, doi, 1998.
- 764 Dellwik, E., Sjöholm, M., and Mann, J.: An evaluation of the WindEye wind lidar, DTU Wind
765 Energy, Report, 2015.
- 766 Fisher, S. G., and Likens, G. E.: Energy flow in Bear Brook, New Hampshire: An integrative
767 approach to stream ecosystem metabolism, *Ecological Monographs*, 43, 421-439, doi:
768 10.2307/1942301, 1973.
- 769 Foken, T.: The energy balance closure problem: An overview, *Ecol. Appl.*, 18, 1351-1367, doi:
770 10.1890/06-0922.1, 2008.
- 771 Frank, J. M., Massman, W. J., and Ewers, B. E.: Underestimates of sensible heat flux due to
772 vertical velocity measurement errors in non-orthogonal sonic anemometers, *Agricultural*
773 *and Forest Meteorology*, 171-172, 72-81, doi: 10.1016/j.agrformet.2012.11.005, 2013.
- 774 Frank, J. M., Massman, W. J., Ewers, B. E., Huckaby, L. S., and Negrón, J. F.: Ecosystem
775 CO₂/H₂O fluxes are explained by hydraulically limited gas exchange during tree
776 mortality from spruce bark beetles, *Journal of Geophysical Research: Biogeosciences*,
777 119, 1195-1215, doi: 10.1002/2013jg002597, 2014.
- 778 Frank, J. M., Massman, W. J., Swiatek, E., Zimmerman, H. A., and Ewers, B. E.: All sonic
779 anemometers need to correct for transducer and structural shadowing in their velocity
780 measurements, *J. Atmos. Ocean. Technol.*, 33, 149-167, doi: 10.1175/jtech-d-15-0171.1,
781 2016.
- 782 Franssen, H. J. H., Stockli, R., Lehner, I., Rotenberg, E., and Seneviratne, S. I.: Energy balance
783 closure of eddy-covariance data: A multisite analysis for European FLUXNET stations,
784 *Agricultural and Forest Meteorology*, 150, 1553-1567, doi:
785 10.1016/j.agrformet.2010.08.005, 2010.

786 Friebel, H. C., Herrington, T. O., and Benilov, A. Y.: Evaluation of the flow distortion around
787 the Campbell Scientific CSAT3 sonic anemometer relative to incident wind direction, *J.*
788 *Atmos. Ocean. Technol.*, 26, 582-592, doi: 10.1175/2008jtecho550.1, 2009.

789 Gelman, A., Carlin, J. B., Stern, H. S., Dunson, D. B., Vehtari, A., and Rubin, D. B.: Bayesian
790 data analysis, Third ed., CRC Press, Boca Raton, FL, 661 pp., 2014.

791 Heilman, J. L., McInnes, K. J., Kjølgaard, J. F., Keith Owens, M., and Schwinning, S.: Energy
792 balance and water use in a subtropical karst woodland on the Edwards Plateau, Texas,
793 *Journal of Hydrology*, 373, 426-435, doi: <http://dx.doi.org/10.1016/j.jhydrol.2009.05.007>,
794 2009.

795 Hogstrom, U., and Smedman, A. S.: Accuracy of sonic anemometers: Laminar wind-tunnel
796 calibrations compared to atmospheric in situ calibrations against a reference instrument,
797 *Bound.-Layer Meteor.*, 111, 33-54, doi: 10.1023/b:boun.0000011000.05248.47, 2004.

798 Horst, T. W., Semmer, S. R., and Maclean, G.: Correction of a non-orthogonal, three-component
799 sonic anemometer for flow distortion by transducer shadowing, *Bound.-Layer Meteor.*, 1-
800 25, doi: 10.1007/s10546-015-0010-3, 2015.

801 Kaimal, J. C., and Businger, J. A.: A continuous wave sonic anemometer-thermometer, *Journal*
802 *of Applied Meteorology*, 2, 156-164, doi: 10.1175/1520-
803 0450(1963)002<0156:acwsat>2.0.co;2, 1963.

804 Kaimal, J. C.: Sonic anemometer measurement of atmospheric turbulence, *Proceedings of the*
805 *Dynamic Flow Conference 1978 on Dynamic Measurements in Unsteady Flows*,
806 Skovlunde, Denmark, 1979, 551-565,

807 Kochendorfer, J., Meyers, T. P., Frank, J. M., Massman, W. J., and Heuer, M. W.: How well can
808 we measure the vertical wind speed? Implications for fluxes of energy and mass, *Bound.-*
809 *Layer Meteor.*, 145, 383-398, doi: 10.1007/s10546-012-9738-1, 2012.

810 Kruschke, J.: *Doing Bayesian data analysis: A tutorial introduction with R and BUGS*, Academic
811 Press, 2010.

812 Lee, X., Finnigan, J. J., and Paw U, K. T.: Coordinate system and flux bias error, in: *Handbook*
813 *of micrometeorology*, edited by: Lee, X., Massman, W. J., and Law, B. E., Kluwer
814 Academic Publishers, Dordrecht, The Netherlands, 33-66, 2004.

815 Leuning, R., van Gorsel, E., Massman, W. J., and Isaac, P. R.: Reflections on the surface energy
816 imbalance problem, *Agricultural and Forest Meteorology*, 156, 65-74, doi:
817 10.1016/j.agrformet.2011.12.002, 2012.

818 Lu, Y., Ye, K., Mathur, A. K., Hui, S., Fuerst, T. P., and Genant, H. K.: Comparative calibration
819 without a gold standard, *Statistics in Medicine*, 16, 1889-1905, doi: 10.1002/(sici)1097-
820 0258(19970830)16:16<1889::aid-sim607>3.0.co;2-v, 1997.

821 MacLean, W. R.: Absolute Measurement of Sound Without a Primary Standard, *The Journal of*
822 *the Acoustical Society of America*, 12, 140-146, doi:
823 doi:<http://dx.doi.org/10.1121/1.1916085>, 1940.

824 Massman, W. J., and Lee, X.: Eddy covariance flux corrections and uncertainties in long-term
825 studies of carbon and energy exchanges, *Agricultural and Forest Meteorology*, 113, 121-
826 144, doi: 10.1016/s0168-1923(02)00105-3, 2002.

827 Monnier, T., Seydou, D., Godin, N., and Zhang, F.: Primary calibration of acoustic emission
828 sensors by the method of reciprocity, theoretical and experimental considerations, *Journal*
829 *of Acoustic Emission*, 30, 152-166, doi, 2012.

830 Nakai, T., and Shimoyama, K.: Ultrasonic anemometer angle of attack errors under turbulent
831 conditions, *Agricultural and Forest Meteorology*, 162–163, 14-26, doi:
832 10.1016/j.agrformet.2012.04.004, 2012.

833 Nakai, T., Iwata, H., Harazono, Y., and Ueyama, M.: An inter-comparison between Gill and
834 Campbell sonic anemometers, *Agricultural and Forest Meteorology*, 195–196, 123-131,
835 doi: 10.1016/j.agrformet.2014.05.005, 2014.

836 Odum, H. T.: Trophic structure and productivity of Silver Springs, Florida, *Ecological*
837 *Monographs*, 27, 55-112, doi: 10.2307/1948571, 1957.

838 Oliphant, A. J., Grimmond, C. S. B., Zutter, H. N., Schmid, H. P., Su, H. B., Scott, S. L., Offerle,
839 B., Randolph, J. C., and Ehman, J.: Heat storage and energy balance fluxes for a
840 temperate deciduous forest, *Agricultural and Forest Meteorology*, 126, 185-201, doi:
841 <http://dx.doi.org/10.1016/j.agrformet.2004.07.003>, 2004.

842 R Core Team: R: A language and environment for statistical computing, 2015,

843 Reba, M. L., Pomeroy, J., Marks, D., and Link, T. E.: Estimating surface sublimation losses from
844 snowpacks in a mountain catchment using eddy covariance and turbulent transfer
845 calculations, *Hydrol. Process.*, 26, 3699-3711, doi: 10.1002/hyp.8372, 2012.

846 RStudio Team: RStudio: Integrated Development for R, 2015,

847 Sathe, A., Mann, J., Gottschall, J., and Courtney, M. S.: Can wind Lidars measure turbulence?, *J.*
848 *Atmos. Ocean. Technol.*, 28, 853-868, doi: 10.1175/jtech-d-10-05004.1, 2011.

849 Scott, R. L., Edwards, E. A., Shuttleworth, W. J., Huxman, T. E., Watts, C., and Goodrich, D. C.:
850 Interannual and seasonal variation in fluxes of water and carbon dioxide from a riparian
851 woodland ecosystem, *Agricultural and Forest Meteorology*, 122, 65-84, doi:
852 <http://dx.doi.org/10.1016/j.agrformet.2003.09.001>, 2004.

853 Stoy, P. C., Mauder, M., Foken, T., Marcolla, B., Boegh, E., Ibrom, A., Arain, M. A., Arneth, A.,
854 Aurela, M., Bernhofer, C., Cescatti, A., Dellwik, E., Duce, P., Gianelle, D., van Gorsel,
855 E., Kiely, G., Knohl, A., Margolis, H., McCaughey, H., Merbold, L., Montagnani, L.,
856 Papale, D., Reichstein, M., Saunders, M., Serrano-Ortiz, P., Sottocornola, M., Spano, D.,
857 Vaccari, F., and Varlagin, A.: A data-driven analysis of energy balance closure across
858 FLUXNET research sites: The role of landscape scale heterogeneity, *Agricultural and*
859 *Forest Meteorology*, 171–172, 137-152, doi:
860 <http://dx.doi.org/10.1016/j.agrformet.2012.11.004>, 2013.

861 Teal, J. M.: Energy flow in the salt marsh ecosystem of Georgia, *Ecology*, 43, 614-624, doi:
862 10.2307/1933451, 1962.

863 Twine, T. E., Kustas, W. P., Norman, J. M., Cook, D. R., Houser, P. R., Meyers, T. P., Prueger,
864 J. H., Starks, P. J., and Wesely, M. L.: Correcting eddy-covariance flux underestimates
865 over a grassland, *Agricultural and Forest Meteorology*, 103, 279-300, doi:
866 10.1016/s0168-1923(00)00123-4, 2000.

867 van der Molen, M. K., Gash, J. H. C., and Elbers, J. A.: Sonic anemometer (co)sine response and
868 flux measurement - II. The effect of introducing an angle of attack dependent calibration,
869 *Agricultural and Forest Meteorology*, 122, 95-109, doi: 10.1016/j.agrformet.2003.09.003,
870 2004.

871 Wahba, G.: Spline interpolation and smoothing on the sphere, *SIAM Journal on Scientific and*
872 *Statistical Computing*, 2, 5-16, doi: doi:10.1137/0902002, 1981.

873 Wang, R., Zhang, Q., Zhao, H., Wang, H., and Wang, C.: Analysis of the surface energy closure
874 for a site in the Gobi Desert in Northwest China, *Acta Meteorologica Sinica*, 26, 250-259,
875 doi: 10.1007/s13351-012-0210-4, 2012.

876 Webb, E. K., Pearman, G. I., and Leuning, R.: Correction of flux measurements for density
877 effects due to heat and water vapour transfer, *Q. J. R. Meteorol. Soc.*, 106, 85-100, doi:
878 10.1256/smsqj.44706, 1980.

879 Welch, C. M., Stoy, P. C., Rains, F. A., Johnson, A. V., and McGlynn, B. L.: The impacts of
880 mountain pine beetle disturbance on the energy balance of snow during the melt period,
881 *Hydrol. Process.*, n/a-n/a, doi: 10.1002/hyp.10638, 2015.

882 Wilson, K., Goldstein, A., Falge, E., Aubinet, M., Baldocchi, D., Berbigier, P., Bernhofer, C.,
883 Ceulemans, R., Dolman, H., Field, C., Grelle, A., Ibrom, A., Law, B. E., Kowalski, A.,
884 Meyers, T., Moncrieff, J., Monson, R., Oechel, W., Tenhunen, J., Valentini, R., and
885 Verma, S.: Energy balance closure at FLUXNET sites, *Agricultural and Forest
886 Meteorology*, 113, 223-243, doi: 10.1016/s0168-1923(02)00109-0, 2002.

887 Wood, S. N.: Generalized additive models: an introduction with R, Chapman and Hall/CRC,
888 2006.

889 Wyngaard, J. C., and Zhang, S.-F.: Transducer-shadow effects on turbulence spectra measured
890 by sonic anemometers, *J. Atmos. Ocean. Technol.*, 2, 548-558, doi: 10.1175/1520-
891 0426(1985)002<0548:tseots>2.0.co;2, 1985.

892 Yahaya, S., and Frangi, J. P.: Cup anemometer response to the wind turbulence-measurement of
893 the horizontal wind variance, *Ann. Geophys.*, 22, 3363-3374, doi: 10.5194/angeo-22-
894 3363-2004, 2004.

895
896

897 Table 1. Summary of the subset of data from Frank et al. (2013) and Frank et al. (2016)
 898 reanalyzed in this study listing the four CSAT3 anemometers (A-D), their location within the
 899 five-position horizontal array, and if mounted horizontally (*). Because processing the Bayesian
 900 model is extremely intensive, only 5% of the available data **were** reanalyzed.

Dates	Position					Number of 5-min periods	
	1	2	3	4	5	Available	Reanalyzed
5-19 July 2011	A*	B	-	C	D*	2,520	126
19-26 July 2011	A	B*	-	C*	D	1,992	100
9-16 August 2011	B*	A	-	D	C*	1,974	98
16-22 August 2011	B	A*	-	D*	C	1,620	81
26-30 July 2013	A*	-	B	-	-	906	46
23-27 August 2013	-	-	A	-	B*	1,050	52
6-24 September 2013	-	-	B	D*	-	498	25

901

902 Table 2. Increase in $H + LE$ (sum of the turbulent components of the energy balance, i.e. sensible
 903 and latent heat flux) at various sites across North America after applying shadow correction to
 904 the CSAT3 time series data.

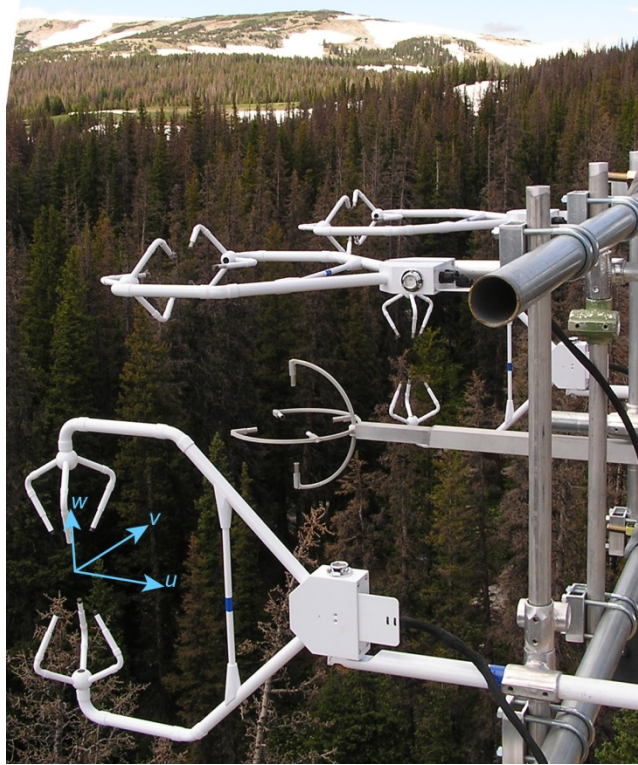
Site	Coordinates	Dates	Height (m)	Percent change after applying shadow correction	
				Kaimal correction	Posterior correction mean \pm standard deviation [95% credible interval]
Yuma, AZ, USA	33° 5' N 114° 32' W	6-15 June 2008	8.25	5.1%	9.8 \pm 2.3% [5.1% 14.8%]
Yuma, AZ, USA	33° 5' N 114° 32' W	5-14 June 2009	2.00	4.5%	9.4 \pm 2.8% [3.1% 16.1%]
Fraser, CO, USA	39° 53' 48.23" N 105° 53' 33.87" W	5-14 April 2015	27.50	5.6%	9.9 \pm 1.4% [7.4% 12.2%]
Fraser, CO, USA	39° 53' 48.23" N 105° 53' 33.87" W	5-14 April 2015	6.40	6.8%	11.6 \pm 1.2% [9.4% 13.9%]
Beltsville, MD, USA	39° 1' 51.23" N 76° 50' 39.40" W	16-31 July 2014	4.00	5.5%	10.4 \pm 2.1% [6.3% 14.8%]
Glacier Peak, WY, USA	41° 22' 52" N 106° 15' 47" W	August-8 September 2015	3.20	5.3%	11.3 \pm 3.1% [4.6% 19.2%]
Agua Salud, Panama	9° 13' 31.65" N 79° 45' 36.41" W	6-16 November 2015	5.00	4.7%	8.1 \pm 1.6% [5.3% 10.8%]

905

906 Table 3. Results of a validation experiment of CSAT3 sonic anemometers at ARDEC, CO
 907 showing the relative error in 5-minute standard deviation of wind (σ) along the cardinal u , v , and
 908 w axes between a vertical instrument and one mounted horizontal and one mounted askew. All
 909 anemometers were compared uncorrected, with the Kaimal correction, and with the posterior
 910 correction.

Manipulation	Cardinal measurement	Root mean square error in σ between a manipulated and vertical anemometer (%)		
		Uncorrected	Kaimal correction	Posterior correction mean \pm standard deviation [95% credible interval]
Horizontal	σ_u	12.6%	8.5%	10.5 \pm 1.3% [8.4% 13.4%]
	σ_v	16.5%	11.4%	9.8 \pm 1.1% [8.0% 12.2%]
	σ_w	15.0%	17.5%	13.4 \pm 1.1% [11.8% 15.9%]
Askew	σ_u	6.7%	4.4%	8.6 \pm 1.5% [6.2% 11.6%]
	σ_v	11.3%	6.0%	10.3 \pm 1.7% [7.2% 13.5%]
	σ_w	14.7%	13.5%	13.9 \pm 2.4% [9.9% 19.4%]

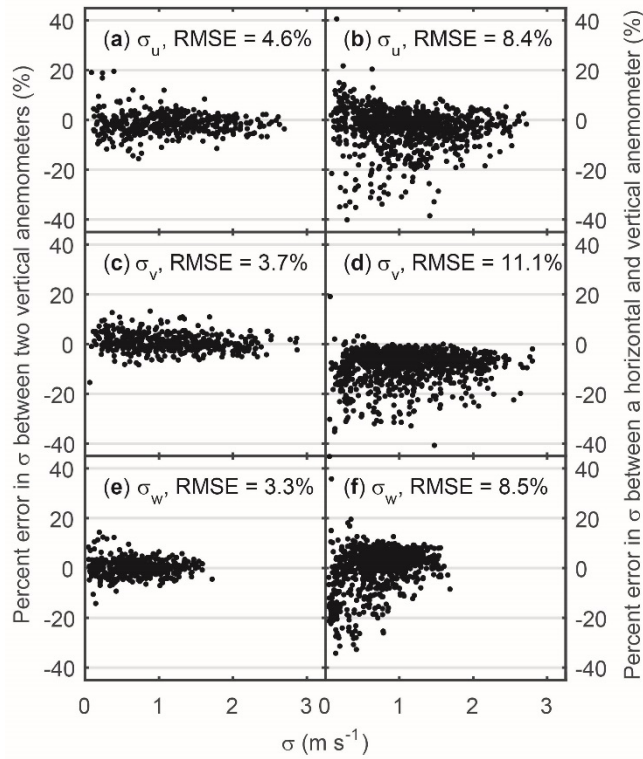
911



912

913 Fig. 1. Photograph of the 2011 experiment with two CSAT3 sonic anemometers mounted
914 vertically and two horizontally. The cardinal u , v , and w axes are shown in light blue near one of
915 the vertical instruments. Figure from Frank et al. (2013).

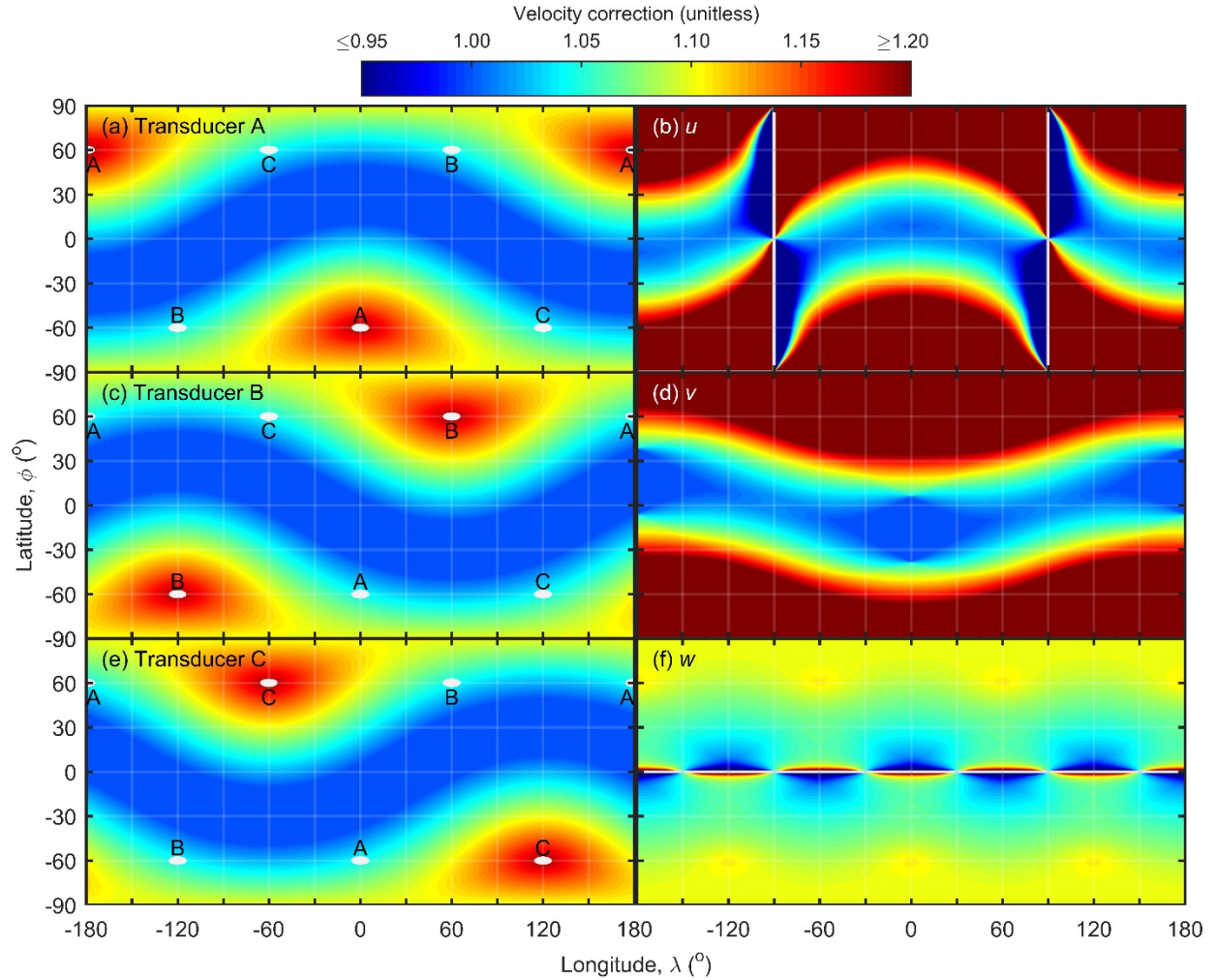
916



917

918 Fig. 2. Uncorrected measurements of the 5-minute standard deviation of wind (σ) along the
 919 cardinal **(a, b)** u , **(c, d)** v , and **(e, f)** w axes are not equivalent between vertically and horizontally
 920 mounted CSAT3 sonic anemometers. Data from an ideal 3D anemometer would have similar
 921 percent errors between a horizontal and a vertical anemometer **(b, d, f)** as found between two
 922 anemometers mounted vertically **(a, c, e)**. The data are from 2011 and 2013 field experiments at
 923 the GLEES AmeriFlux site (Frank et al., 2016; Frank et al., 2013). The 2011 data in panels **b, d,**
 924 and **f** are randomly paired between the two anemometers in different orientations. Results are
 925 summarized as root mean square error (RMSE).

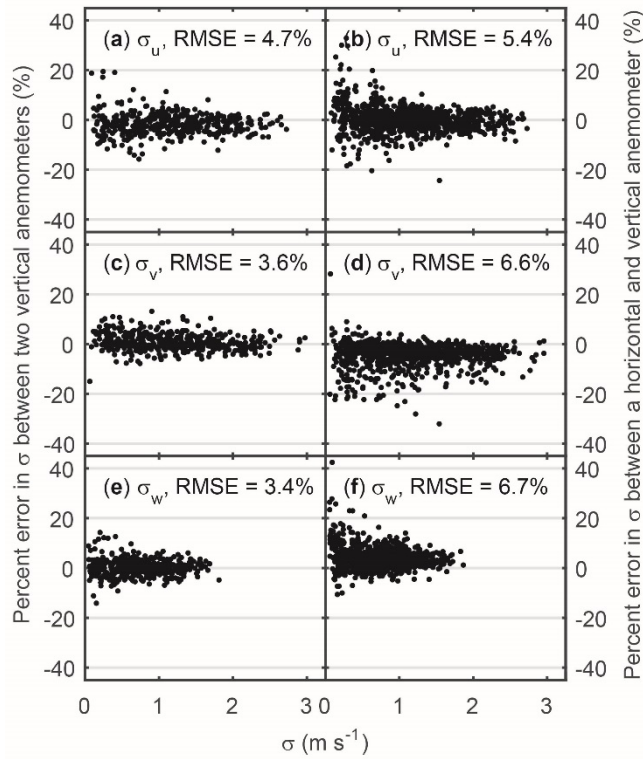
926



927

928 Fig. 3. The Kaimal correction, one of three priors tested in this study, for the (a) A, (c) B, and (e)
 929 C transducer pairs, each represented by a white dot, of a CSAT3 sonic anemometer accounts for
 930 self-shadowing but not cross-shadowing between transducers. The same correction expressed in
 931 sonic anemometer coordinates (b) u , (d) v , and (f) w shows that for near-equatorial winds,
 932 minimal correction is required for the horizontal wind components while significant correction
 933 and instability exist in the vertical wind component w . Longitude and latitude are relative to the u
 934 axis (Fig. 1).

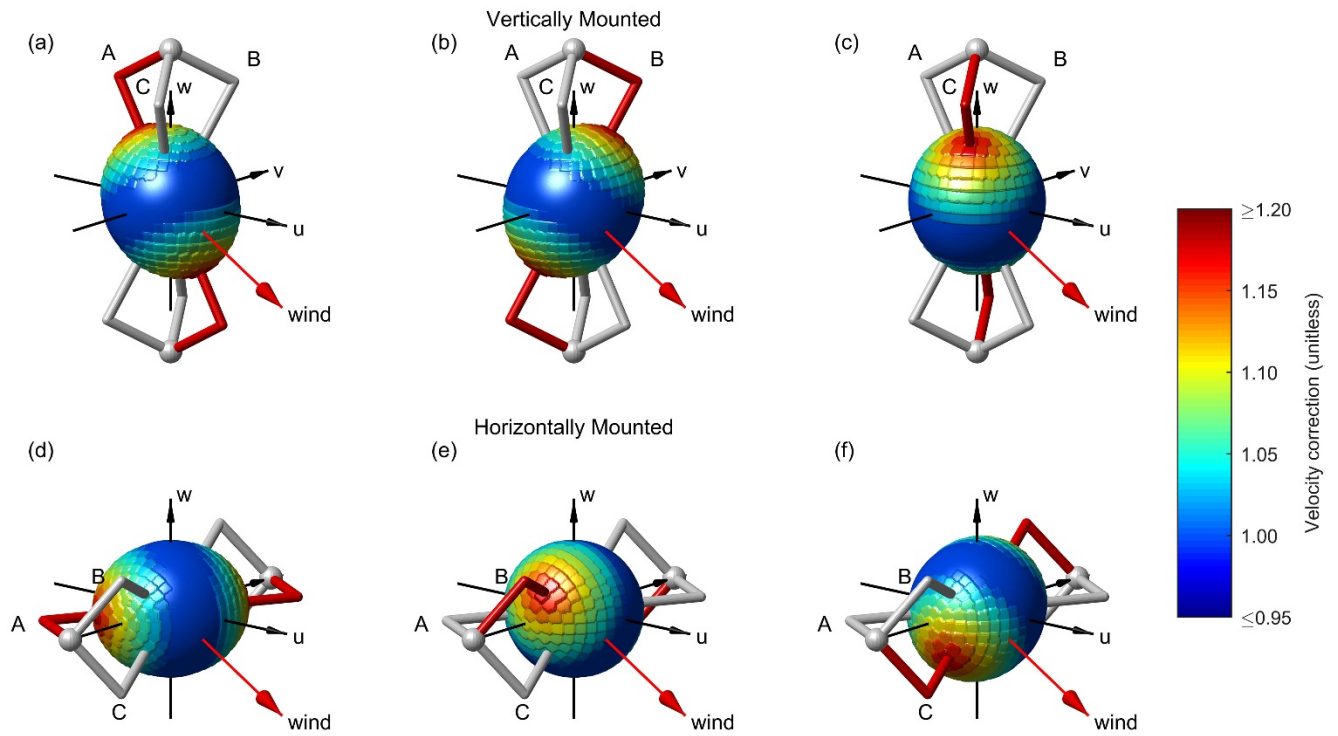
935



936

937 Fig. 4. Kaimal corrected measurements (i.e. one of three priors tested) of the 5-minute standard
 938 deviation of wind (σ) along the cardinal **(a, b)** u , **(c, d)** v , and **(e, f)** w axes are more equivalent
 939 between vertically and horizontally mounted sonic anemometers. The percent errors between a
 940 horizontal and a vertical anemometer **(b, d, f)** are smaller for all three cardinal dimensions than it
 941 was for the uncorrected data (Fig. 2) being more similar to those found between two
 942 anemometers mounted vertically **(a, c, e)**. The data are from 2011 and 2013 field experiments at
 943 the GLEES AmeriFlux site (Frank et al., 2016; Frank et al., 2013). The 2011 data in panels **b, d,**
 944 and **f** are randomly paired between the two anemometers in different orientations. Results are
 945 summarized as root mean square error (RMSE).

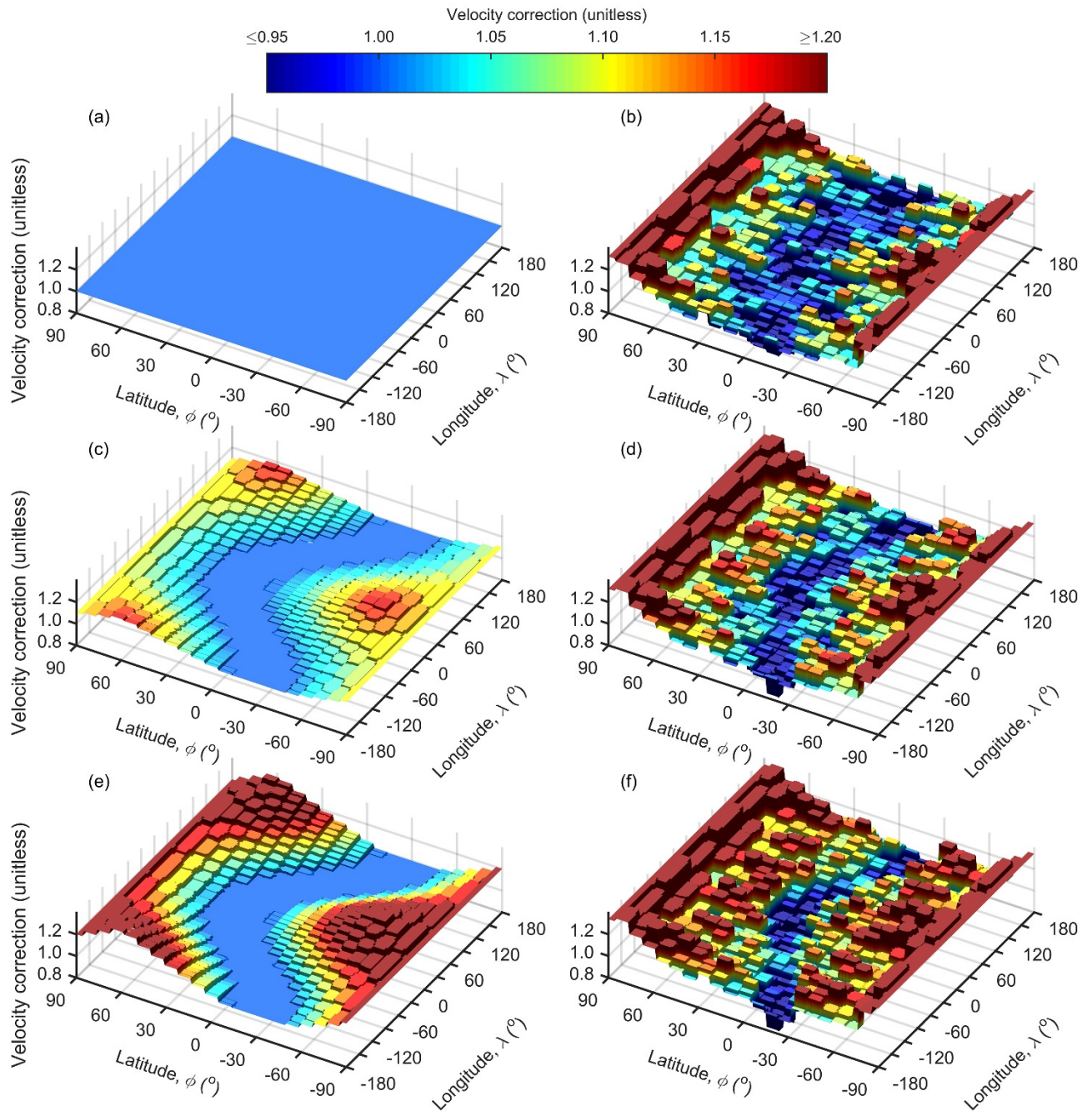
946



947

948 Fig. 5. The Kaimal correction, one of three priors tested in this study, evaluated among 512 cells
 949 for the (a, d) A, (b, e) B, and (c, f) C transducer pairs of the CSAT3 sonic anemometer mounted
 950 either in the (a-c) typically vertical or (d-f) experimentally horizontal orientations. Though the
 951 correction is identical relative to all transducer pairs, the same instantaneous wind results in
 952 different corrections depending on the transducer pair and the orientation.

953

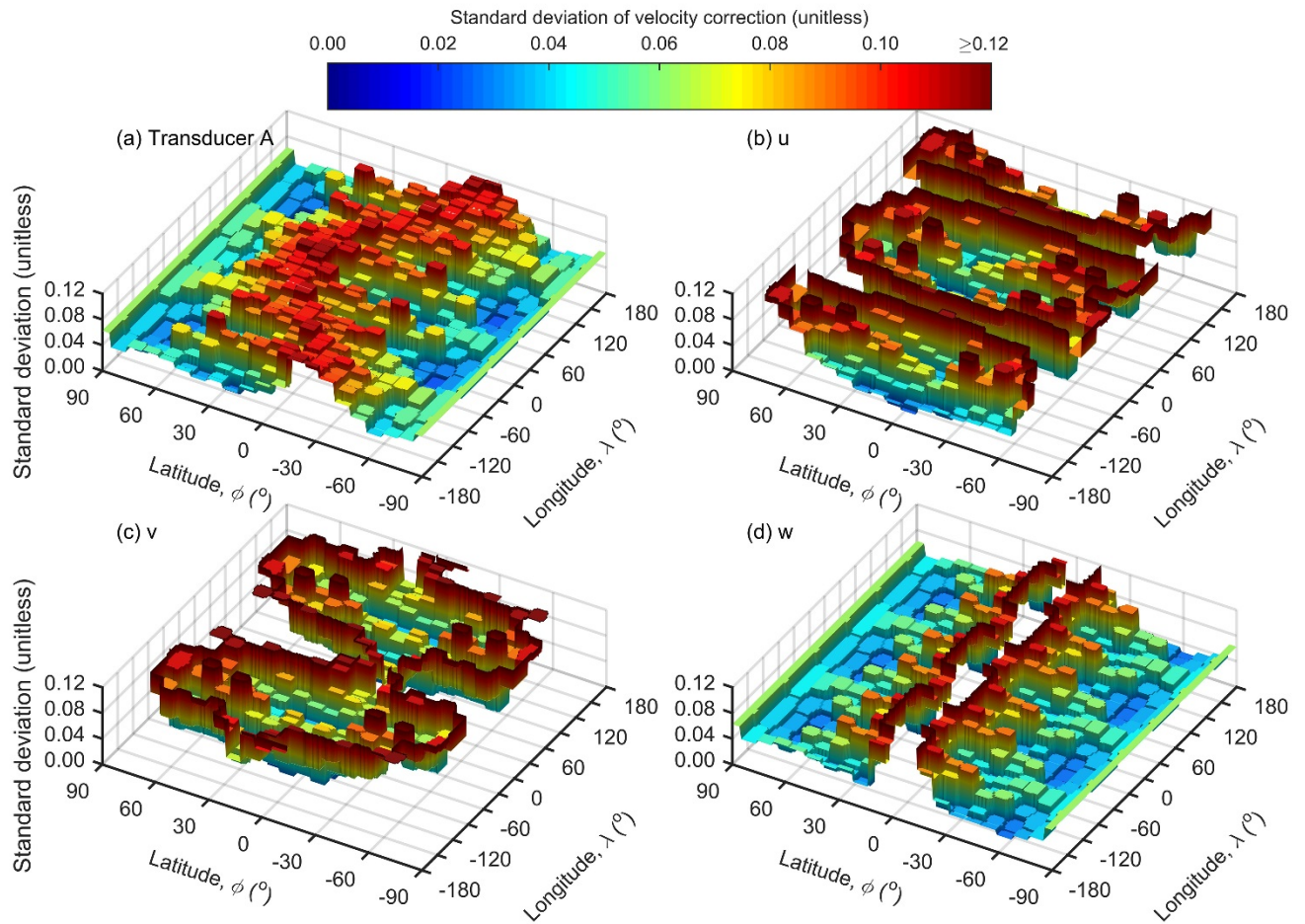


954

955 Fig. 6. The A transducer pair correction evaluated among 512 cells for the three prior corrections
 956 tested in this study, (a) flat, (c) Kaimal, and (e) double-Kaimal, with their corresponding
 957 unnormalized posterior corrections (b), (d), and (f), respectively. All posteriors have similar
 958 relative topography. They differ in absolute scaling where priors with higher absolute magnitude

959 result in posteriors with higher absolute magnitude, which is apparent from the different
960 colorings.

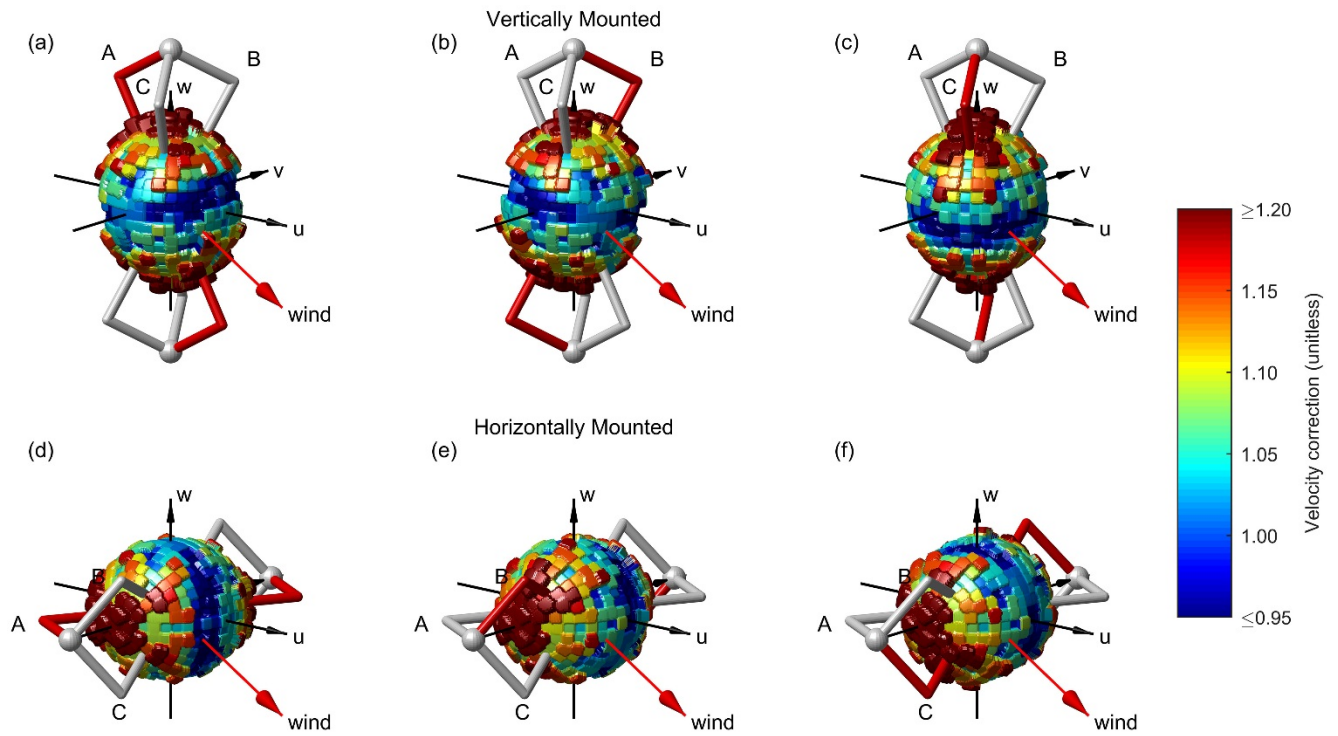
961



962

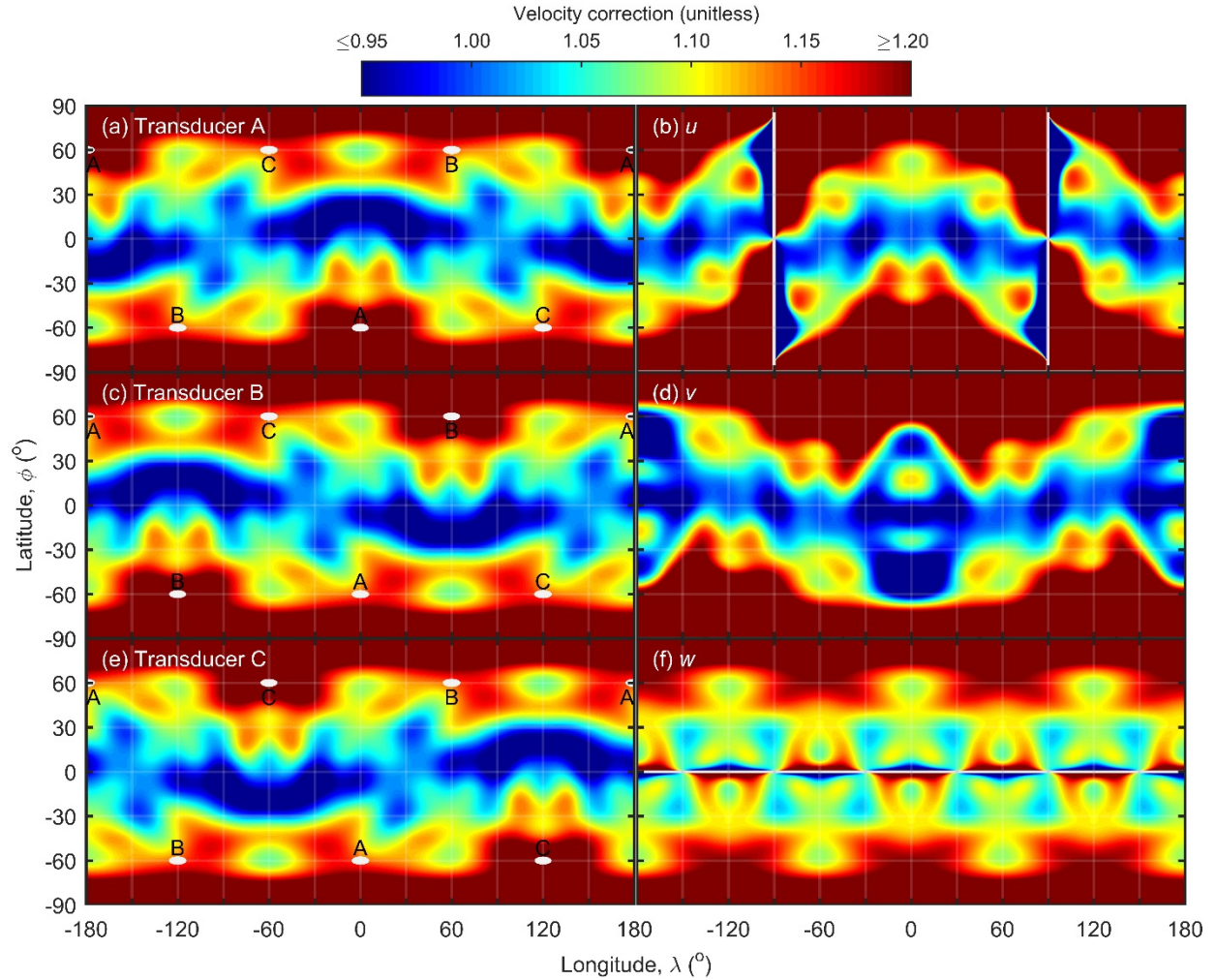
963 Fig. 7. Standard deviations of the posterior correction for (a) the A transducer pair and the wind
 964 velocities (b) u , (c) v , and (d) w . When compared to the standard deviation of the prior which
 965 was defined as 0.1, the transducer correction is more certain in regions with higher topography
 966 (Fig. 6). The results in CSAT3 sonic coordinates reflect both the uncertainty in the transducer
 967 correction plus cancelation and amplification of errors due to the coordinate transformation. The
 968 posterior correction for u , v , and w is most certain for winds along the u , v , and w -axes,
 969 respectively.

970



971
 972 Fig. 8. The posterior correction evaluated for the (a, d) A, (b, e) B, and (c, f) C transducer pairs
 973 of the CSAT3 sonic anemometer mounted either in the (a-c) typically vertical or (d-f)
 974 experimentally horizontal orientations. The correction is identical relative to all transducer pairs
 975 and is constructed from 512 cells with 138 unique values. The Bayesian model adjusts these
 976 values to simultaneously correct the same instantaneous wind measured from different
 977 transducer pairs and orientations in order to produce similar cardinal u , v , and w wind statistics
 978 (Fig. 10).

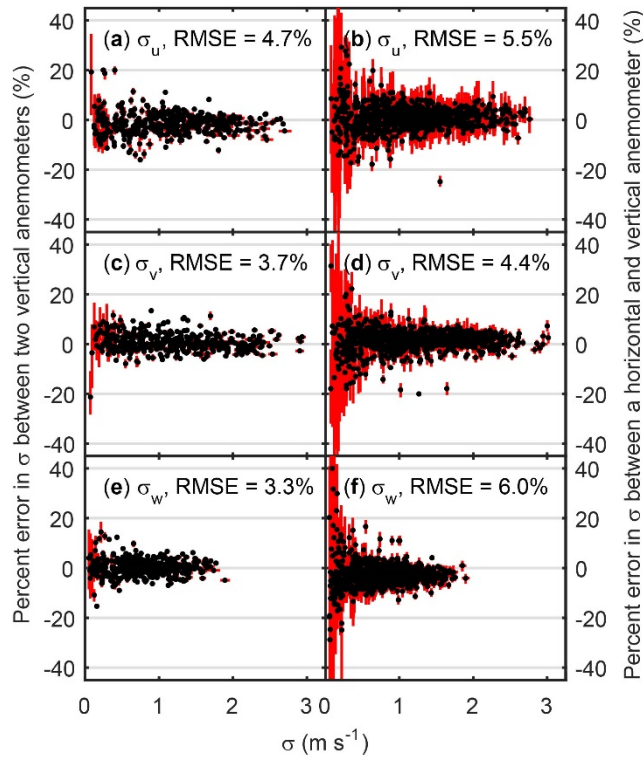
979



980

981 Fig. 9. The posterior correction for the (a) A, (c) B, and (e) C transducer pairs, each represented
 982 by a white dot, of a CSAT3 sonic anemometer accounts for both self-shadowing and cross-
 983 shadowing between transducers. The same correction expressed in sonic anemometer
 984 coordinates (b) u , (d) v , and (f) w shows that for near-equatorial winds, minimal correction is
 985 required for the horizontal wind components while even more correction exists in the vertical
 986 wind component w than was present with the Kaimal correction (Fig. 3f). Longitude and latitude
 987 are relative to the u axis (Fig. 1).

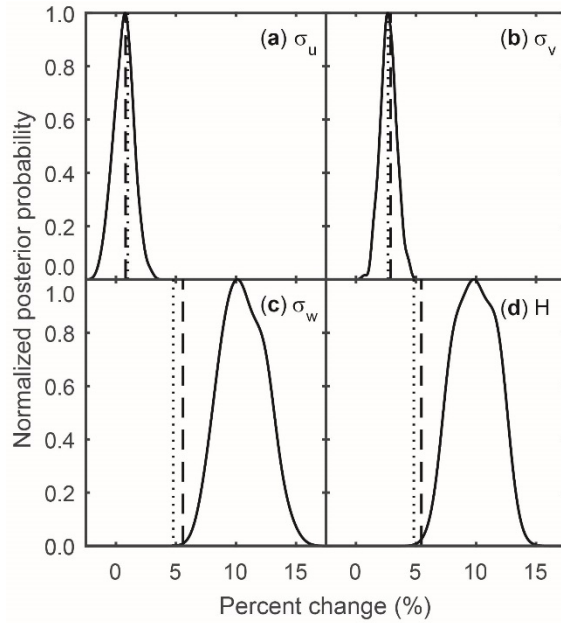
988



989

990 Fig. 10. Posterior corrected measurements of the 5-minute standard deviation of wind (σ) along
 991 the cardinal **(a, b)** u , **(c, d)** v , and **(e, f)** w axes are most equivalent between vertically and
 992 horizontally mounted sonic anemometers than with either the uncorrected (Fig. 2) or Kaimal
 993 corrected data (Fig. 4). The percent errors between a horizontal and a vertical anemometer are
 994 small **(b, d, f)**, especially for the cardinal v -dimension **(d)**, and are similar to those found
 995 between two anemometers mounted vertically **(a, c, e)**. The data are from 2011 and 2013 field
 996 experiments at the GLEES AmeriFlux site (Frank et al., 2016; Frank et al., 2013). The 2011 data
 997 in panels **b, d, and f** are randomly paired between the two anemometers in different orientations.
 998 Results are summarized as root mean square error (RMSE). The red lines are 95% credible
 999 intervals.

1000



1001
 1002 Fig. 11. Though application of the Kaimal (dashed lines) and posterior (solid lines) corrections
 1003 result in similar changes to the 5-minute standard deviations of wind (σ) along the **(a)** u and **(b)** v
 1004 axes, application of the posterior correction results in significantly higher (95% credible interval)
 1005 **(c)** winds along the w axis and **(d)** sensible heat flux (H). The dotted lines are an alternate
 1006 formulation of the Kaimal correction proposed by Wyngaard and Zhang (1985) and used in
 1007 Horst et al. (2015). Data are for vertically mounted anemometers only.
 1008